frontiers | Frontiers in Earth Science

TYPE Original Research
PUBLISHED 15 December 2022
DOI 10.3389/feart.2022.990761

OPEN ACCESS

EDITED BY
Hervé Rezeau,
University of Arizona, United States

REVIEWED BY
Hadi Shafaii Moghadam,
Damghan University, Iran
Michael Schirra,
Université de Genève, Switzerland

*CORRESPONDENCE
Hossein Kouhestani,
kouhestani@znu.ac.ir

SPECIALTY SECTION
This article was submitted to Economic Geology,
a section of the journal
Frontiers in Earth Science

RECEIVED 10 July 2022
ACCEPTED 06 December 2022
PUBLISHED 15 December 2022

CITATION
Kouhestani H, Mokhtari MAA, Chang Z, Qin K and Aghajani Marsa S (2022), Fluid inclusion, zircon U-Pb geochronology, and O-S isotopic constraints on the origin and evolution of ore-forming fluids of the tashvir and varmazyar epithermal base metal deposits, NW Iran.
Front. Earth Sci. 10:990761.
doi: 10.3389/feart.2022.990761

Fluid inclusion, zircon U-Pb geochronology, and O-S isotopic constraints on the origin and evolution of ore-forming fluids of the tashvir and varmazyar epithermal base metal deposits, NW Iran

Hossein Kouhestani[1]*, Mir Ali Asghar Mokhtari[1], Zhaoshan Chang[2,3], Kezhang Qin[4,5] and Soheila Aghajani Marsa[6]

[1]Department of Geology, Faculty of Sciences, University of Zanjan, Zanjan, Iran, [2]Department of Geology and Geological Engineering, Colorado School of Mines, Golden, CO, United States, [3]EGRU (Economic Geology Research Centre), College of Science and Engineering, James Cook University, Townsville, QLD, Australia, [4]Key Laboratory of Mineral Resources, Institute of Geology and Geophysics, Chinese Academy of Sciences, Beijing, China, [5]University of Chinese Academy of Sciences, Beijing, China, [6]Mineralogy Laboratories, Iranian Mineral Processing Research Center (IMPRC), Karaj, Iran

Tashvir and Varmazyar deposits are part of the epithermal ore system in the Tarom–Hashtjin Metallogenic Belt (THMB), NW Iran. In both deposits, epithermal veins are hosted by Eocene volcanic-volcaniclastic rocks of the Karaj Formation and are spatially associated with late Eocene granitoid intrusions. The ore assemblages consist of pyrite, chalcopyrite, chalcocite, galena, and sphalerite (Fe-poor), with lesser amounts of bornite and minor psilomelane and pyrolusite. Fluid inclusion measurements from the Tashvir and Varmazyar revealed 182–287 and 194–285°C formation temperatures and 2.7–7.9 and 2.6–6.4 wt.% NaCl equivalent salinities, respectively. The oxygen isotope data suggested that the mineralizing fluids originated dominantly from a magmatic fluid that mixed with meteoric waters. The sulfur isotope data indicated that the metal and sulfur sources were largely a mixture of magma and surrounding sedimentary rocks. LA-ICP–MS zircon U–Pb dating of the granitoid intrusion at Tashvir and Varmazyar, yielded a weighted mean age of 38.34–38.31 and 40.85 Ma, respectively, indicating that epithermal mineralization developed between 40.85 and 38.31 Ma. Our data indicated that fluid mixing along with some fluid boiling were the main drives for hydrothermal alteration and mineralization at Tashvir and Varmazyar. All these characteristics suggested an intermediate-sulfidation epithermal style of mineralization. The THMB is proposed to be prospective for precious and base metal epithermal mineralization. Considering the extensional tectonic setting, and lack of advanced argillic lithocaps and hypersaline fluid inclusions, the THMB possibly has less potential for economically important porphyry mineralization.

KEYWORDS

intermediate-sulfidation, fluid inclusions, stable isotopes, geochronology, NW Iran

1 Introduction

Epithermal deposits have various styles of mineralization characteristics, alteration, and ore mineral assemblage, and are classified as high-sulfidation (HS), intermediate-sulfidation (IS), and low-sulfidation (LS) types (White and Hedenquist, 1990; Cooke and Simmons, 2000; Hedenquist et al., 2000; Qin et al., 2002; Einaudi et al., 2003; Sillitoe and Hedenquist, 2003; Gemmell, 2004; Simmons et al., 2005). These deposits are commonly associated with subaerial volcanism and calc-alkaline to alkaline intrusions that formed in island arcs and continental arcs at convergent plate margins, as well as in intra-arc, back-arc, and post-collisional rift settings (White and Hedenquist, 1990; Cooke and Simmons, 2000; John, 2001; Sillitoe and Hedenquist, 2003; Simmons et al., 2005). The Alpine–Himalayan Orogenic Belt (AHOB) hosts numerous small-to large-sized porphyry Cu–Mo (Au), orogenic Au, epithermal Au, and Pb–Zn–Cu (Ag), and skarn Fe and polymetallic deposits (e.g., Hou and Wang, 2008; Xie et al., 2017; Richards, 2015; Hou and Zhang, 2015; Kouhestani et al., 2015; Moritz et al., 2016a, b; Searle et al., 2016; Mokhtari et al., 2019). The Tarom–Hashtjin Metallogenic Belt (THMB) is located in the central part of the AHOB (Figure 1A). As a part of the AHOB, the THMB was formed associated with Cenozoic closures of the Neo-Tethyan oceanic branches, i.e., Khoy–Zanjan ocean, and related microcontinental collisions (e.g., Azizi and Jahangiri, 2008; Asiabanha and Foden, 2012; Castro et al., 2013). The THMB is one of the most significant metallogenic belts in northwestern Iran and hosts many epithermal precious and base metal deposits and occurrences, such as Nikoueieh, Marshoun, Zajkan, Zehabad, Khalyfehlou, Chargar, Abbasabad, Chodarchay, Tashvir, Aliabad-Khanchy, Lubin-Zardeh, Aqkand, Jalilabad, Gulojeh, Varmazyar, Chomalou, and Shah Ali Beiglou (Figure 1B; Esmaeli et al., 2015; Mehrabi et al., 2016; Kouhestani et al., 2017; 2018a; 2019a; b, 2020, 2022; Yasami et al., 2017, 2018; Mikaeili et al., 2018; Yasami and Ghaderi, 2019; Mousavi Motlagh and Ghaderi, 2019; Mousavi Motlagh et al., 2019, 2021; Shahbazi et al., 2019; Zamanian et al., 2019; Ghasemi Siani et al., 2022). These deposits are mostly hosted by Eocene volcanic-volcaniclastic rocks of the Karaj Formation and generally cluster around the late Eocene granitoid intrusions which are thought to be genetically related (Ghasemi Siani et al., 2015; Mehrabi et al., 2016; Kouhestani et al., 2018a). On the basis of the sulfidation states, epithermal precious and base metal deposits in the THMB belong to three subtypes: 1) HS (i.e., Chodarchay and north Gulojeh deposits), 2) IS (i.e., Abbasabad, Zehabad, Zajkan, Marshoun, Lubin-Zardeh, Aliabad-Khanchy, south Gulojeh, Jalilabad, Aqkand, Chomalou, and Shah Ali Beiglou deposits), and 3) LS (i.e., Nikoueieh, Khalyfehlou, and Chargar deposits).

The Tashvir and Varmazyar deposits are two small-scale epithermal base metal deposits located in the middle and northwestern parts of the THMB, respectively. According to a 2016 exploration report, the Tashvir deposit has a proven ore resource of 0.12 Mt with average grades of 1.5% Cu, 3% Pb + Zn, and 15 g/t Ag (Kouhestani, 2016). The Varmazyar deposit contains a proven ore resource of 0.10 Mt, grading at 3.1% Pb, 1.6% Zn, and 32 g/t Ag (Karimpouli, 2017). Both deposits are expected to be revealed as medium-sized deposits by more detailed exploration. The Varmazyar deposit has close spatial relationships with late Eocene granitoid intrusions, which provide a good case for studying the relationship between epithermal mineralization and late Eocene magmatism at THMB. The ore deposit geology, mineralogy, and whole-rock geochemistry of the Tashvir and Varmazyar deposits were conducted in previous studies, that were published in Persian (e.g., Kouhestani and Mokhtari, 2019; Ghorbani, 2020; Ghorbani et al., 2022). They argued that the Tashvir and Varmazyar deposits are probably IS-type epithermal mineralization. Nevertheless, little is known about the source of ore-forming fluids and materials and mineralization processes, and no specific information and age data about the relationship between mineralization and granitoid intrusions were reported. As a result, the mineralization type of these deposits is not well understood, which limits the better understanding of their ore-forming mechanism and genesis.

Based on detailed field investigations of the geological characteristics, fluid inclusion (FI) microthermometry, O–S isotopic geochemical analysis, and LA-ICP–MS zircon U–Pb dating of the granitoid intrusions, we discuss the ore genesis of the Tashvir and Varmazyar deposits and the relationship between epithermal mineralization and late Eocene magmatism in the THMB. The results provide helpful information about the mineralization processes of epithermal precious and base metal deposits in the THMB and give a new direction for further exploration in this belt and northwest Iran.

2 Geology and mineralization of the tashvir and varmazyar deposits

Geology and mineralization characteristics of the Tashvir and Varmazyar deposits have been documented in previous studies (e.g., Faridi and Anvari, 2000; Amini et al., 2001; Kouhestani and Mokhtari, 2019; Ghorbani et al., 2022) and

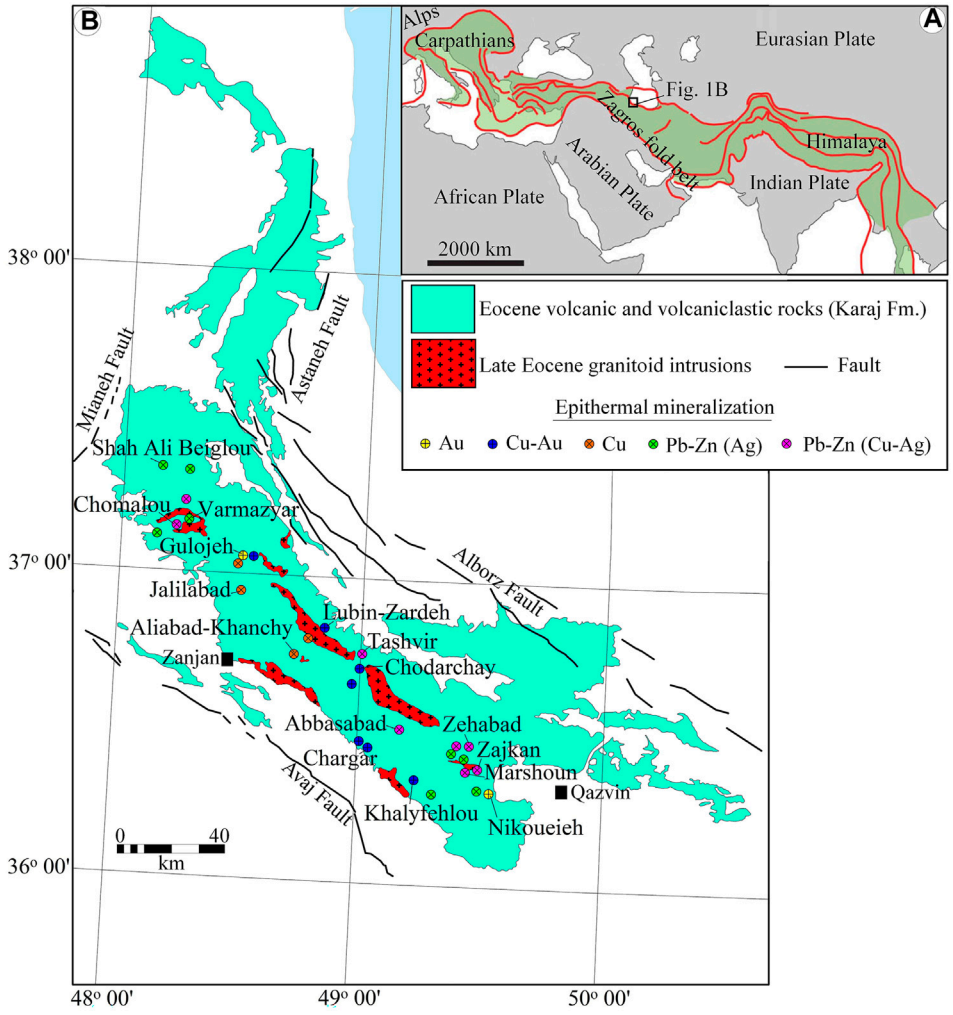

FIGURE 1
(A). Tectonic sketch map of the Alpine–Himalayan Orogenic Belt (AHOB) showing the location of the Tarom–Hashtjin Metallogenic Belt (THMB) in northwest Iran (modified after Johnson, 2021). **(B)**. Simplified regional geology of the THMB (modified from 1:100,000 geological maps of Iran, Geological Survey of Iran) showing distribution of the Tashvir, Varmazyar, and other epithermal precious and base metal deposits.

the following summaries are from Kouhestani and Mokhtari (2019), and Ghorbani et al. (2022), as well as our field observations.

2.1 Tashvir deposit

The exposed strata at Tashvir include Eocene volcanic and volcaniclastic rocks of the Karaj Formation, and Oligo-Miocene, Miocene, and Plio-Quaternary sedimentary rocks (Figure 2, Kouhestani and Mokhtari, 2019). The Eocene Karaj Formation is widely distributed in the Tashvir area. It is the main strata hosting the ore veins and is composed mainly of tuff (i.e., lithic tuff, crystal tuff, and lithic crystal tuff), ignimbrite, sandy tuff, tuffaceous sandstone, and shale, with interbedded lava flows of andesite, andesitic basalt, and rhyolite-rhyodacite. The Oligo-Miocene strata unconformably overlie or are in fault contact with the Karaj Formation and comprise tuffaceous claystone, siltstone, and conglomerate. The Miocene strata consist mainly of marl, calcareous sandstone, claystone, and local conglomerate. The Plio-Quaternary rocks are less developed in the Tashvir area. They are predominantly composed of loosely cemented, polygenetic, locally marly conglomerates. Parallel and angular unconformities are observed in the contacts between the Oligo-Miocene strata and overlying Miocene strata and the Plio-Quaternary rocks, respectively. Exposed intrusive bodies at Tashvir include only late Eocene granitoid intrusion intrudes into the Eocene Karaj Formation in the southern periphery of the area (Figure 2). It is mainly composed of quartz monzonite, quartz syenite, granite,

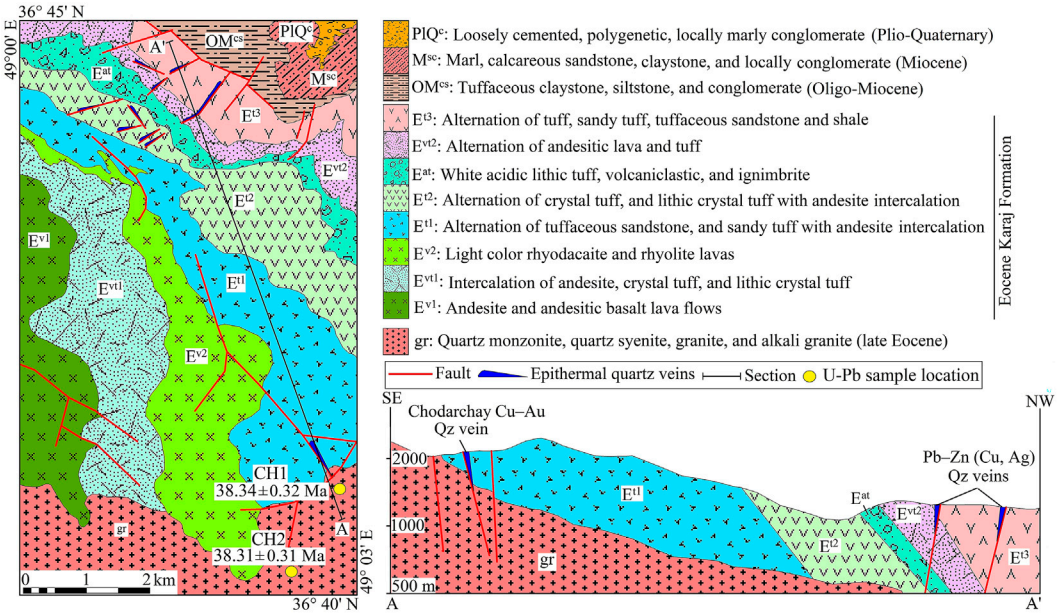

FIGURE 2
Geological map of the Tashvir Pb–Zn (Cu–Ag) deposit (modified from Kouhestani and Mokhtari, 2019).

and alkali granite, and is closely associated to the Chodarchay Cu–Au epithermal deposit (Yasami et al., 2017, 2018; Yasami and Ghaderi, 2019).

NE- and NW-trending faults are the main faults present within the Tashvir deposit (Figure 2), both of them hosting the ore veins in the northern part. The NE-trending faults are the main ore-controlling structures consisting of a series of faults trending from N15 to N75 E, with dips ranging from 50° to 85°. The NW-trending faults trend from N20 to N40 W, with dip angles of 80–85° or nearly vertical.

Orebodies at Tashvir occur mainly as irregular quartz-sulfide veins along NE- and NW-trending faults in the volcanic-volcaniclastic units (E^{t2}, E^{vt2}, and E^{t3} units) of the Eocene Karaj Formation (Figures 2, 3A). A total of nine Pb–Zn (Cu–Ag) quartz veins were explored (Kouhestani and Mokhtari, 2019). Seven of these veins strike northeast, with dips in northwestward or southeastward directions at 50°–85°. Two other veins trend northwest to southeast and dip steeply (~85°) to the northeast. The length and thickness of the ore veins are various, ranging from 25 to 300 m and from 0.75 to 3 m, respectively. The ore veins have similar morphology, sharp contact with their wall rocks, and are enveloped by 1–2 m width intermediate argillic alteration haloes (Figure 3B). Sheeted and stockwork quartz-sulfide veinlets are found around the main veins within the hydrothermal alteration haloes (Figure 3C).

The ore minerals in the Tashvir deposit are essentially chalcopyrite, chalcocite, galena, and sphalerite (Fe-poor), with lesser bornite (Figures 3D–F). Silver is not visible and is hosted by galena. The ore minerals occur in veins, vein breccias, stockworks, and breccia infill, and also as dissemination in altered wall rocks. The principal gangue minerals are quartz, calcite, and chlorite with vein-veinlet, vug infill, colloform/crustiform banding, and plumose textures (Figures 3G–I). On the basis of the mineral assemblages, ore textures, and crosscutting relationships, four paragenetic stages of mineralization are distinguished at Tashvir (Figure 4, Kouhestani and Mokhtari, 2019): 1) quartz-polymetallic sulfide (chalcopyrite–chalcocite–galena–sphalerite ± bornite) stage, 2) quartz stage, 3) calcite stage, and 4) chlorite stage. These stages are overprinted by a supergene oxidized zone characterized by covellite, smithsonite, cerussite, malachite, and goethite near the surface.

The hydrothermal alteration is chiefly distributed along and in the locality of fracture zones which are filled by the quartz-sulfides and, or calcite and chlorite. Quartz, sericite–illite (intermediate argillic), carbonate, and chlorite types of hydrothermal alteration occur close to the ore veins (10 cm–~2 m from veins), whereas pervasive sericite–epidote–chlorite–calcite (propylitic) alteration occurs at farther away locations (Kouhestani and Mokhtari, 2019).

2.2 Varmazyar deposit

The Varmazyar deposit is hosted by a series of Eocene volcanic and volcaniclastic strata of the Karaj Formation that

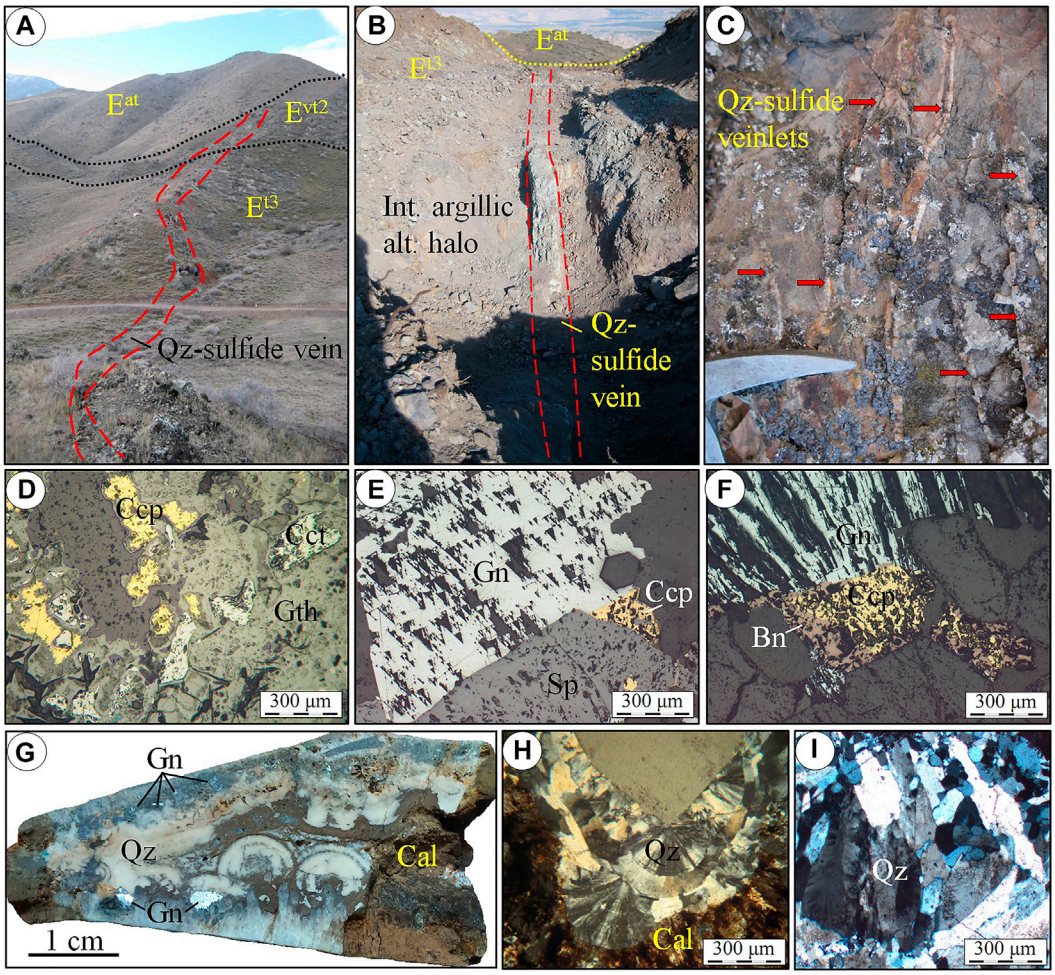

FIGURE 3
Photographs are showing characteristics of the ore veins, mineralogy, and textures at the Tashvir deposit. Images in **(D–F)** are from polished blocks in reflected light, while H and I are taken in transmitted light, XPL. **(A)**. General view of the main quartz-sulfide vein hosted by the E^{t3} and E^{vt2} units of the Karaj Formation, looking northeast. **(B)**. Quartz-sulfide vein surrounded by 2 m wide intermediate argillic alteration halo, looking northeast. **(C)**. Sheeted mineralized quartz-sulfide veins (red arrows) within the hydrothermal alteration haloes of the main ore veins. **(D)**. Anhedral chalcopyrite is intergrown with chalcocite. **(E)**. Subhedral coarse-grained galena intergrowth with sphalerite and chalcopyrite. Sphalerite enclosed chalcopyrite inclusions. **(F)**. Galena intergrowth with chalcopyrite. Chalcopyrite was replaced by bornite. **(G,H)**. Colloform/crustiform texture of quartz vein. Calcite fills the vugs. **(I)**. Quartz veins with plumose texture. Bn: bornite, Br: braunite, Cal: calcite, Ccp: chalcopyrite, Cct: chalcocite, Cer: cerussite, Gn: galena, Gth: goethite, Lith: tuff fragment, Py: pyrite, Pyr1: primary pyrolusite, Pyr2: secondary pyrolusite, Ps: psilomelane, Qz: quartz, Sm: smithsonite, Sp: sphalerite. Mineral abbreviations follow Whitney and Evans (2010).

were intruded by late Eocene intrusions (Figure 5, Ghorbani et al., 2022). The Karaj Formation can be subdivided into two units in ascending sequence. Unit one is dominated by alternating intermediate lithic tuff, lithic-crystal tuff, and crystal tuff with andesite, basaltic andesite, and basalt intercalations. Unit two is mainly composed of an alternation of acidic lithic tuff, lithic-crystal tuff, and crystal tuff with some rhyodacite intercalation. The intrusive rock in this area consists of the Haji Seyran pluton that is exposed mainly in the southern parts of the Varmazyar area (Figure 5). It ranges in composition from monzogranite to syenogranite and is composed of plagioclase (10–30%), K-feldspar (35–60%), quartz (15–20%), biotite (5–10%), and some hornblende (5%), with coarse-to medium-grained porphyritic to porphyroidic and granular textures. The accessory minerals are clinopyroxene, sphene, apatite, and zircon. The main structures in the Varmazyar area are N- and NE-trending faults (Figure 5). The NS-trending faults are the critical ore control faults that dip 65°–85° westward. The NE-trending faults trend from N20 to N40 E, with dip ranging from 60 to 75°.

Pb–Zn (Ag) mineralization at Varmazyar occurred as an asymmetrical quartz-sulfide brecciated vein that occupies an

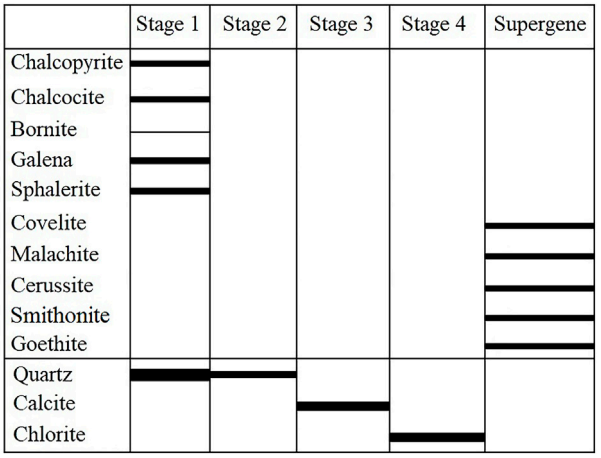

FIGURE 4
Simplified sequence of mineral paragenesis in the Tashvir deposit (after Kouhestani and Mokhtari, 2019).

Galena, sphalerite (Fe-poor), pyrite, psilomelane, and pyrolusite are the principal ore minerals; smithsonite, cerussite, goethite, secondary pyrolusite, and braunite are supergene minerals (Figures 6E–H). Silver is not visible and is hosted by galena. The main gangue phases include quartz and calcite. The ore and gangue minerals formed as vein-veinlet, vein breccias, and breccia infill, and show disseminated, vein-veinlet, brecciated, comb, colloform/crustiform, cockade, bladed, plumose, and vug infill textures (Figures 6I–L). According to ore textures and crosscutting relationships, mineral assemblages, and paragenetic sequence, at least four mineralization stages are identified in the Varmazyar deposit (Figure 7, Ghorbani et al., 2022): 1) pre-ore quartz-pyrite stage, 2) quartz-galena-sphalerite-minor pyrite stage, 3) quartz-calcite (Cal I)-manganese oxides-hydroxides (psilomelane, pyrolusite) stage, and 4) barren post-ore calcite (Cal II) stage. These stages are overprinted by a supergene oxidized zone near the surface.

Wall-rock alteration is zoned. The quartz, sericite–illite (intermediate argillic), and carbonate alteration occurs close to the ore veins (5 cm–~2 m from veins), while the sericite–

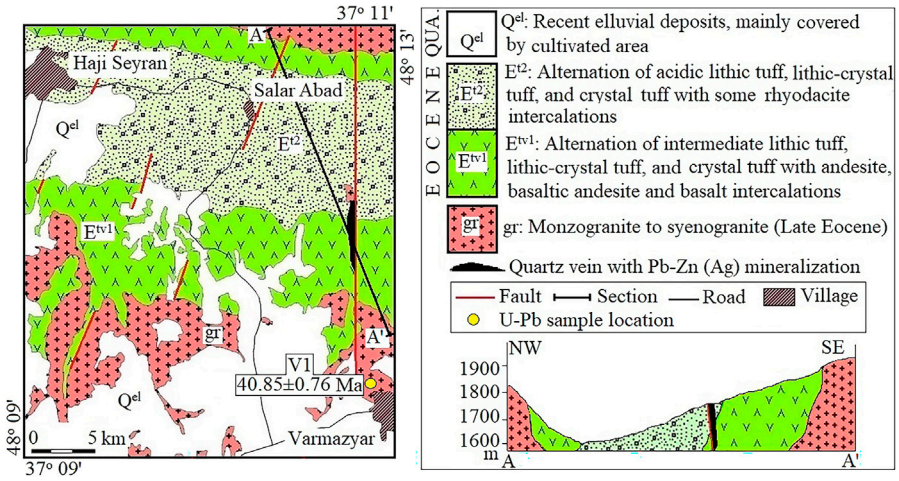

FIGURE 5
Geological map of the Varmazyar Pb–Zn (Ag) deposit (modified after Ghorbani et al., 2022).

N-trending fault in the volcanic-volcaniclastic units (E^{tv1} and E^{t2} units) of the Eocene Karaj Formation (Figures 5, 6A). The Pb–Zn (Ag) ore vein has up to 300 m in length and 2–3 m in width and is usually dipping to the west at 65°–80° with about 150–200 m down-dip extensions (Ghorbani et al., 2022). It has clear contact with its wall rocks and is covered by a ~2 m width intermediate argillic alteration halo in the hanging wall (Figures 6B,C). In some parts of the deposit, later Mn-bearing quartz-calcite vein-veinlets crosscut the primary Pb–Zn (Ag) ore vein (Figure 6C).

epidote–calcite–chlorite (propylitic) alteration occurs at a greater distance (Ghorbani et al., 2022).

3 Sampling and methods

3.1 U–Pb zircon geochronology

Three samples, including quartz monzonite and granite intrusions at Tashvir and monzogranite body at Varmazyar,

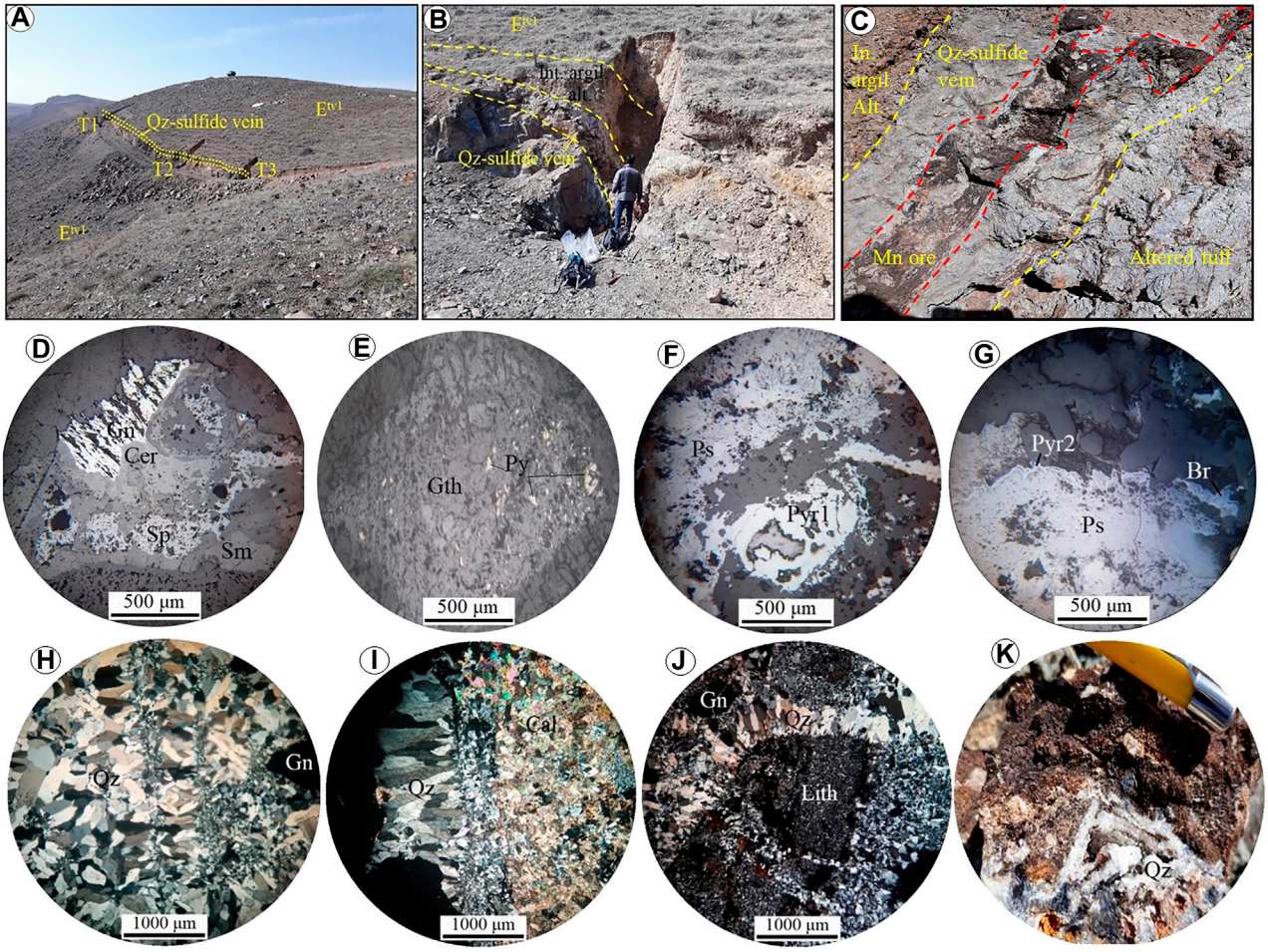

FIGURE 6
Photographs are showing features of the ore veins, mineralogy, and textures at the Varmazyar deposit. Images in **(D–G)** are from polished blocks in reflected light, while **(H–J)** are taken in transmitted light, XPL. **(A)**. General view of the quartz-sulfide ore vein hosted by the E^{tv1} unit of the Karaj Formation, looking southwest. **(B)**. Quartz-sulfide ore vein covered by 2 m wide intermediate argillic alteration halo in the hanging wall, looking west. **(C)**. Quartz-sulfide ore vein crosscutting by Mn-bearing quartz-calcite veins. **(D)**. Intergrowth of galena and sphalerite. Both minerals, respectively, altered to cerussite and smithsonite along boundaries. **(E)**. Anhedral pyrite crystal altered to goethite. **(F)**. Intergrowth of psilomelane and primary pyrolusite. **(G)**. Anhedral to subhedral psilomelane crystals altered to secondary pyrolusite and braunite along boundaries. **(H,I)**. Crustiform texture of quartz in quartz-sulfide **(H)** and quartz-calcite **(I)** veinlets. In I, the plumose texture of quartz is also observed. **(J)**. Cockade texture of quartz developed around tuff fragments. **(K)**. Lattice-bladed calcite was replaced by quartz along with colloform texture of quartz. Abbreviations as in Figure 3.

were selected for U–Pb zircon geochronology (Figures 2, 5). Zircons are obtained from crushed rocks by handpicking under the binocular microscope after sieving and conventional heavy-liquid and magnetic separation techniques at the Langfang Hongxin Geological Exploration Technology Service Co. Ltd., Langfang, China. The internal structure of zircon was examined using cathodoluminescence (CL) prior to U-Pb isotope analysis. CL imaging and U-Pb dating were both undertaken at the University of Tasmania, Hobart, Australia. The analyses were completed with an Agilent 7500cs quadrupole ICP–MS with a 193 nm coherent Ar-F gas laser and a Resonetics M50 ablation cell. The spot diameter was 29 µm. The LA-ICP–MS analysis followed the procedure described by Meffre et al. (2008). The downhole fractionation, instrument drift, and mass bias correction factors for U–Pb ratios on zircons were calculated using two analyses on the primary (91,500 standards of Wiendenbeck et al., 1995) and one analysis on each of the secondary (TEMORA standard of Black et al. (2003) and GJ1 standard of Jackson et al. (2004)) standard zircons analyzed at the beginning of the session and every 12 unknown zircons (roughly every 1/2 h) using the same spot size and conditions as used on the samples. Additional

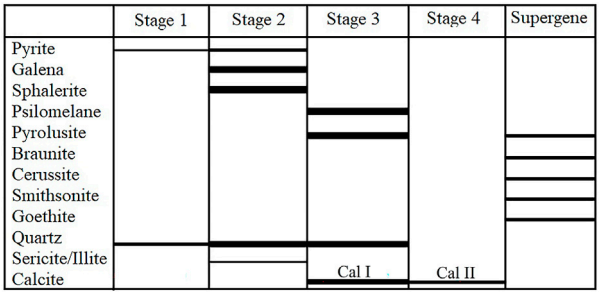

FIGURE 7
Paragenetic sequence of ore and gangue minerals at the Varmazyar deposit (after Ghorbani et al., 2022).

secondary standards (the Mud Tank zircon of Black and Gulson, 1978) were also analyzed. The correction factor for the $^{207}Pb/^{206}Pb$ ratio was calculated using three large spots of NIST-610 analyzed at the beginning and end and corrected using the values recommended by Baker et al. (2004). Element abundances on zircons were calculated, using the method outlined by Kosler (2001) using Zr as the internal standard element, assuming stoichiometric proportions, and using the 91,500 to standardize correction for mass bias. Isoplot 3.00 (Ludwig, 1998) was used for plotting radiogenic isotope data and for U–Pb age calculation. Age data are reported at 1σ errors, whereas the uncertainties for Concordia plots and weighted mean ages are given at a 95% confidence level (2σ).

3.2 Fluid inclusion systematics

Fifteen doubly polished thick (~150 μm) sections including crystallized quartz and honey-colored (Fe-poor) sphalerite were prepared for FI analysis. Detailed petrographic observations with specific emphasis on applying the fluid inclusion assemblages (FIAs) concept (Goldstein and Reynolds, 1994; Goldstein, 2003) were first carried out to evaluate the shapes and types, distributions, and liquid/vapor ratios of FIs. Microthermometric analysis used a Linkam THMSG-600 heating–freezing stage (−196 to +600 °C) mounted in a ZEISS microscope at the FI laboratory of Iranian Mineral Processing Research Center (IMPRC), Karaj, Iran. The heating-freezing rate is commonly 3–5°C/min with an accuracy of ±0.5°C, nevertheless condensed to less than 0.2°C/min close to the phase transition with an accuracy of ±0.1°C. The stage was calibrated according to the melting points of the cesium nitrate (414°C) and n-hexane (−94.3°C) with precisions of ±0.6°C for heating and ±0.2°C for freezing measurements. Salinities (wt.% NaCl equivalent) of the aqueous inclusions were calculated based on final ice-melting points (Bodnar, 1993). The program sowatflinc_inclusion version 2007 (Driesner and Heinrich, 2007) was used to calculate densities (g/cm^3) and P-T data.

3.3 O–S isotopes

Samples for stable isotope studies were collected from mineralized veins and breccias. Mineral aggregates were handpicked under a binocular microscope with a purity of >99%. Oxygen isotope analyses (five quartz and two calcite) were performed at the National Isotope Centre, New Zealand. The oxygen isotopic analysis of quartz was undertaken using a laser extraction technique with BrF_5 as the reagent. Isotope measurements, performed on molecular oxygen, were modified after the technique of Sharp (1990). Samples were heated using a CO_2 laser, and the isotope analyses were performed using a Europa Geo 20–20 stable isotope ratio mass spectrometer in dual inlet mode. Samples and standards were heated overnight to 150 °C before loading into the vacuum extraction line, where they were evacuated for ~6 h. Blank BrF_5 runs were carried out until the yield was <0.2 μ-moles oxygen. Results are reported in δ notation relative to Vienna-Standard Mean Ocean Water (V-SMOW) using $\delta^{18}O$ values of +9.6‰ and +5.8‰ for standards NBS-28 and UWG-2 Garnet, respectively. The reproducibility was better than ±0.15‰.

Calcite was analyzed on the GVI IsoPrime Carbonate Preparation System at a reaction temperature of 60°C and analyzed using a dual inlet on the IsoPrime mass spectrometer. The result is reported concerning VPDB (Vienna Pee Dee Belemnite), normalized to internal standards GNS marble, with reported values of −6.40‰ VPDB for $\delta^{18}O$. The oxygen isotope value was converted to $\delta^{18}O_{SMOW}$ and expressed as $\delta^{18}O_{SMOW} = 1.03092 \times \delta^{18}O_{VPDB} + 30.92$. This analysis provides $\delta^{18}O$ with a precision of ±0.15‰.

Sulfur isotope measurements (n=12) were performed using the conventional methods of Robinson and Kusakabe (1975) on an Isoprime100 mass spectrometer coupled to an Elementar varioPYRO cube elemental analyzer at the Central Science Laboratory, University of Tasmania (Hobart, Australia). Calibration was based on the internal (homogenous galena from Broken Hill and Rosebery) and international (IAEA-S-1, -S-2, -S-3, -S-4, and -SO_5, plus NBS-123 and -127) reference standards with known isotopic composition. All results are reported in standard notation $\delta^{34}S$ relative to the Cañon Diablo Troilite (CDT). The analytical precision is ±0.2‰ (1σ) in the laboratory.

4 Results

4.1 U–Pb zircon geochronology

The LA-ICP–MS U–Pb data of zircons from Tashvir and Varmazyar are listed in Table 1. Most zircons are concordant to near-concordant and have limited variation in isotopic composition, resulting inclusters Wetherill Concordia diagrams (Figure 8). The quartz monzonite sample (CH1) at Tashvir yielded a Concordia age of 38.34 ± 0.32 Ma (MSWD = 0.71; Figure 8A) based on fourteen concordant data points. One concordant single-grain analysis (CH1-

TABLE 1 LA-ICP–MS zircon U–Pb age data of granitoid intrusions from the Tashvir and Varmazyar deposits.

	^{207} cor^{206}Pb/^{238}U		^{206}Pb/^{238}u		^{208}Pb/^{232}Th		^{207}Pb/^{206}Pb		Content (ppm)			
	Age	±1 ster	ratio	±1 RSE%	ratio	±1 RSE%	ratio	±1 RSE%	Hf	Pb (total)	Th	U
CH1-1	37	0.5	0.0058	1.3	0.0019	3.2	0.0473	3.2	13,317	9	827	1,007
CH1-2	38	0.7	0.0059	1.8	0.0020	4.6	0.0508	6.2	9,743	3	226	244
CH1-3	38	0.6	0.0059	1.6	0.0020	4.3	0.0462	5.4	10,308	4	325	418
CH1-4	38	0.7	0.0060	1.8	0.0022	4.9	0.0608	5.4	11,117	4	229	308
CH1-5	38	0.6	0.0060	1.6	0.0019	4.4	0.0491	5.5	10,929	3	187	290
CH1-6	38	0.8	0.0074	1.9	0.0056	3.6	0.2045	3.4	9,819	4	152	197
CH1-7	38	0.6	0.0059	1.5	0.0019	3.9	0.0434	5.0	11,173	4	346	396
CH1-8	38	0.6	0.0060	1.5	0.0019	3.5	0.0464	4.1	11,816	6	496	602
CH1-9	39	0.7	0.0060	1.7	0.0019	4.0	0.0502	5.8	9,859	4	262	314
CH1-10	39	0.7	0.0060	1.8	0.0019	4.3	0.0474	6.1	10,390	3	242	265
CH1-11	39	0.7	0.0060	1.7	0.0020	4.0	0.0467	5.7	10,228	4	291	340
CH1-12	39	0.6	0.0060	1.5	0.0019	5.0	0.0443	5.8	10,921	4	232	337
CH1-13	39	0.6	0.0061	1.6	0.0020	4.0	0.0506	6.3	11,176	4	290	331
CH1-14	39	0.6	0.0061	1.6	0.0019	3.7	0.0455	5.6	12,159	4	327	411
CH1-15	39	0.9	0.0061	2.2	0.0020	6.2	0.0450	8.7	9,523	2	91	130
CH2-1	37	0.5	0.0058	1.4	0.0019	3.8	0.0468	4.3	10,943	6	403	624
CH2-2	38	0.5	0.0059	1.3	0.0023	4.1	0.0469	2.3	15,085	16	255	2,194
CH2-3	38	0.5	0.0059	1.4	0.0020	2.9	0.0482	2.7	10,665	12	1,005	1,387
CH2-4	38	0.6	0.0059	1.5	0.0021	5.0	0.0496	3.3	11,814	8	199	1,039
CH2-5	38	0.5	0.0059	1.4	0.0020	3.6	0.0454	4.0	11,522	6	437	618
CH2-6	38	0.6	0.0059	1.4	0.0020	4.0	0.0484	5.1	10,810	5	335	466
CH2-7	38	0.7	0.0060	1.7	0.0020	4.8	0.0504	5.1	9,281	4	248	370
CH2-8	38	0.5	0.0060	1.4	0.0019	3.2	0.0461	3.3	9,917	10	793	1,141
CH2-9	39	0.6	0.0060	1.4	0.0018	3.7	0.0436	4.4	11,419	6	326	610
CH2-10	39	0.5	0.0060	1.3	0.0019	3.1	0.0470	2.9	9,305	10	934	1,056
CH2-11	39	0.6	0.0060	1.4	0.0019	3.7	0.0459	3.3	11,633	7	433	819
CH2-12	39	0.9	0.0061	2.3	0.0020	6.8	0.0463	6.8	11,719	3	125	288
CH2-13	39	0.6	0.0061	1.6	0.0021	4.2	0.0484	3.9	11,018	5	325	486
CH2-14	41	0.6	0.0063	1.5	0.0020	3.9	0.0484	5.1	10,541	5	291	436
CH2-15	41	0.9	0.0064	2.3	0.0022	8.3	0.0488	7.6	9,425	7	465	653
V1-1	39	0.5	0.0061	1.4	0.0021	4.1	0.0563	3.9	8,905	6	429	518
V1-2	39	0.7	0.0061	1.7	0.0020	4.2	0.0534	6.2	8,536	4	283	301
V1-3	40	1.0	0.0062	2.5	0.0022	6.4	0.0437	12.5	9,316	2	77	81
V1-4	40	0.7	0.0063	1.6	0.0020	4.3	0.0472	7.2	9,148	3	216	232
V1-5	41	0.9	0.0065	2.1	0.0024	5.7	0.0683	8.4	8,269	3	163	171

(Continued on following page)

TABLE 1 (*Continued*) LA-ICP–MS zircon U–Pb age data of granitoid intrusions from the Tashvir and Varmazyar deposits.

	^{207} cor^{206}Pb/^{238}U		^{206}Pb/^{238}u		^{208}Pb/^{232}Th		^{207}Pb/^{206}Pb		Content (ppm)			
V1-6	41	0.8	0.0064	1.9	0.0022	4.8	0.0515	6.2	10,369	3	179	203
V1-7	41	0.8	0.0064	1.8	0.0021	4.0	0.0445	6.3	9,113	3	249	264
V1-8	41	0.9	0.0064	2.2	0.0022	5.9	0.0423	7.8	8,957	3	126	156
V1-9	42	0.9	0.0064	2.1	0.0022	4.5	0.0457	7.5	7,464	3	238	171
V1-10	42	0.6	0.0067	1.4	0.0025	3.2	0.0702	3.8	10,203	6	462	498
V1-11	42	0.8	0.0070	1.8	0.0031	5.6	0.1024	7.1	8,051	3	170	181
V1-12	42	0.9	0.0065	2.1	0.0022	4.6	0.0477	7.0	9,683	3	214	198
V1-13	42	0.7	0.0066	16	0.0022	3.4	0.0480	5.0	9,410	4	502	296
V1-14	42	0.9	0.0066	2.2	0.0020	6.5	0.0504	8.6	9,697	2	123	141
V1-15	44	0.8	0.0067	1.7	0.0020	4.5	0.0435	6.2	8,536	3	318	227

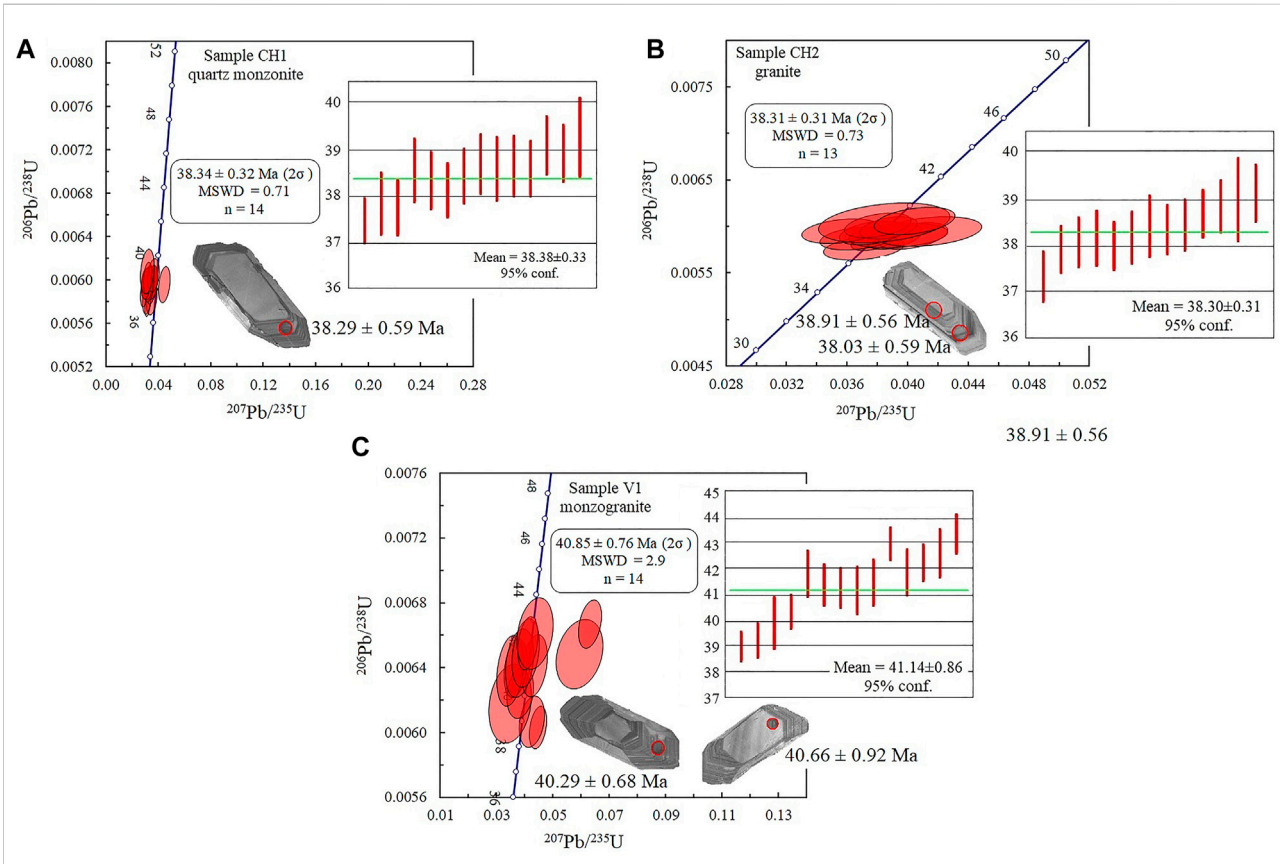

FIGURE 8
Zircon U–Pb Wetherill Concordia diagrams and representative CL images for granitoid intrusions in the Tashvir **(A,B)** and Varmazyar **(C)** deposits. Mean ^{206}Pb/^{238}U ages are reported with 2σ errors. MSWD = mean square weighted deviation. N = number of spot analyses.

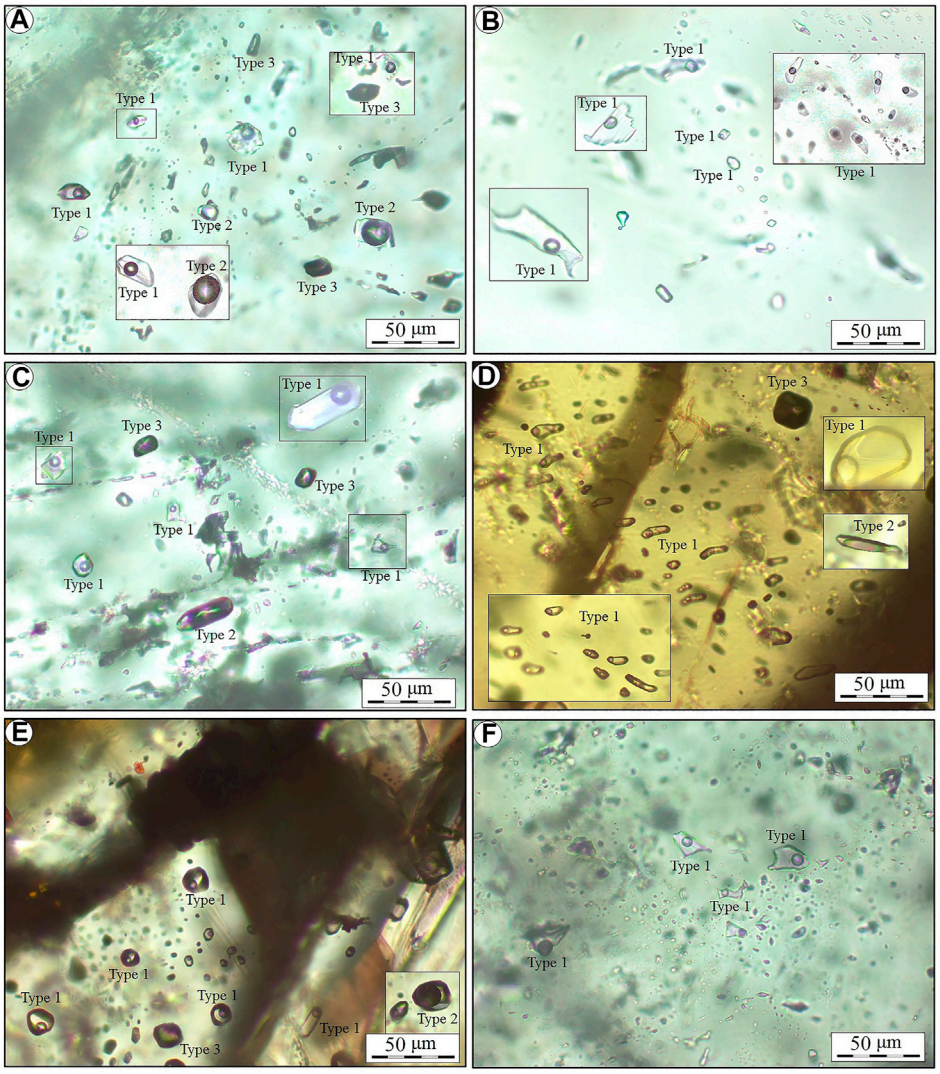

FIGURE 9
Representative photomicrographs are showing different FI types and assemblages in quartz and sphalerite from the Tashvir and Varmazyar epithermal base metal deposits. **(A)**. Coexistence of types 1 and 2 inclusions together with type 3 inclusions hosted by quartz from ore-stage 1 at Tashvir. **(B)**. Random, and scattered distribution of type 1 inclusions hosted by quartz from ore-stage 2 at Tashvir. C–E. Assemblages of types 1, 2, and 3 FIs hosted by quartz **(C)** and sphalerite **(D,E)** from ore-stage 2 at Varmazyar. **(F)**. Type 1 inclusions within quartz of ore-stage 3 at Varmazyar. Note that FIs enclosed in the rectangles are from different depths and are brought to focus as insets.

6, Table 1) yielded a Concordia age of 38.25 ± 0.84 Ma. This grain has a bigger uncertainty on its $^{206}Pb/^{238}U$ ratio and is not shown in the Concordia diagram of Figure 8A. The Concordia age of the granite sample (CH2) from Tashvir is 38.31 ± 0.31 Ma (MSWD = 0.73; Figure 8B) based upon thirteen concordant data points. This age is identical within error to the age of the concordant zircons in the quartz monzonite sample. Two separate zircons from sample CH2 (CH2-14 and CH2-15, Table 1), however, yielded older Concordia ages of 41 ± 0.63 Ma and 41 ± 0.95 Ma. These zircons were presumably xenocrysts derived locally from the Eocene volcanic-volcaniclastic rocks that had been incorporated into the melt. These two grains were excluded from the Concordia age and diagram of sample CH2. Fourteen concordant zircons from the monzogranite sample (V1) at Varmazyar gave a Concordia age at 40.85 ± 0.76 (MSWD = 2.9; Figure 8C). One zircon (V1-15, Table 1) yielded a discordant analysis that pointed to an inherited component of a 44 ± 0.75 Ma age. This grain was omitted from the Concordia age and is not shown in the Concordia diagram of Figure 8C. Overall, the LA-ICP–MS U–Pb dating of zircons from the Tashvir and Varmazyar deposits are in line with regional

TABLE 2 Microthermometric data for primary type 1 fluid inclusion assemblages from Tashvir and Varmazyar deposits.

		Host mineral	n	Size (μm)	Vapor (vol%)	$T_{m\text{-}ice}$ (°C)	T_h (°C)	Salinity (wt.% NaCl equivalent)	ρ (g/cm^3)
Tashvir	Quartz-polymetallic sulfide stage (ore-stage 1)								
		Quartz	4	10–15	15–25	−2.5 ± 0.3	239 ± 10	4.2 ± 0.2	0.85
			2	17–18	15–20	−1.5 ± 0.1	245 ± 7	2.6 ± 0.8	0.83
			4	9–12	10–15	−2.8 ± 0.4	227 ± 11	4.7± 0.4	0.87
			5	9–15	10–20	−4.4 ± 0.5	223 ± 15	7.0 ± 0.8	0.90
			7	9–12	20–30	−2.7 ± 0.4	221 ± 10	4.5 ± 0.6	0.88
			1	10	25	−4.0	190	6.4	0.93
			4	9–30	10–15	−2.2 ± 0.8	218 ± 10	3.7 ± 0.5	0.87
			4	5–20	15–25	−3.0 ± 0.6	224 ± 15	5.0 ± 0.9	0.88
			4	5–15	20–30	−5.0 ± 0.4	228 ± 13	7.9 ± 0.7	0.90
			3	9–12	10–15	−2.5 ± 0.3	228 ± 12	4.2 ± 0.6	0.87
			4	5–15	15–25	−3.4 ± 0.8	287 ± 5	5.6 ± 0.8	0.80
			3	8–12	20–25	−1.9 ± 0.9	186 ± 15	3.2 ± 0.7	0.91
			3	10–18	25–30	−3.4 ± 0.8	195 ± 11	5.6 ± 0.8	0.91
			4	5–16	10–15	−2.6 ± 0.4	220 ± 10	4.3 ± 0.7	0.88
			2	8–10	15–20	−3.0 ± 0.7	240 ± 12	5.6 ± 0.9	0.86
			4	8–10	15–25	−2.8 ± 0.6	205 ± 18	4.6± 0.6	0.90
	Quartz stage (ore-stage 2)								
		Quartz	2	12–22	15–20	−1.6 ± 0.5	163 ± 9	2.7 ± 0.8	0.92
			3	12–18	15–25	−0.7 ± 0.3	154 ± 6	1.3 ± 0.7	0.92
			6	8–12	20–30	−0.5 ± 0.5	159 ± 9	0.9 ± 0.8	0.92
			4	10–18	15–20	−1.0 ± 0.2	169 ± 8	1.7 ± 0.6	0.91
			3	12–35	25–30	−1.1 ± 0.4	154 ± 7	1.8 ± 0.4	0.93
			4	8–15	10–20	−0.5 ± 0.5	161 ± 10	0.9 ± 0.8	0.91
			3	8–15	10–15	−1.3 ± 0.3	173 ± 10	2.2 ± 0.4	0.91
			3	9–12	20–25	−0.7 ± 0.5	172 ± 12	1.2 ± 0.7	0.90
			3	8–10	15–25	−0.7 ± 0.6	168 ± 8	1.2 ± 0.9	0.91
			3	8–10	10–15	−0.3 ± 0.7	162 ± 9	0.5 ± 0.3	0.91
			3	10–18	15–20	−0.6 ± 0.8	130 ± 5	1.0 ± 0.8	0.94
			5	8–28	15–25	−1.0 ± 0.3	157 ± 7	1.8 ± 0.8	0.92
			5	5–18	10–15	−1.0 ± 0.5	148 ± 7	1.8 ± 0.6	0.93
			4	8–16	15–25	−1.1 ± 0.9	182 ± 5	1.8 ± 0.8	0.90
			4	5–12	15–20	−1.0 ± 0.7	173 ± 12	1.7 ± 0.9	0.91
Varmazyar	Quartz-galena- sphalerite-minor pyrite stage (ore-stage 2)								
		Quartz	4	10–20	10–15	−2.8 ± 0.4	214 ± 9	4.6± 0.4	0.89
			4	5–15	10–15	−3.2 ± 0.6	203 ± 14	5.3 ± 0.6	0.90

(Continued on following page)

TABLE 2 (*Continued*) Microthermometric data for primary type 1 fluid inclusion assemblages from Tashvir and Varmazyar deposits.

		Host mineral	n	Size (μm)	Vapor (vol%)	$T_{m\text{-}ice}$ (°C)	T_h (°C)	Salinity (wt.% NaCl equivalent)	ρ (g/cm^3)
			3	5–8	15–25	−2.3 ± 0.5	207 ± 11	3.8 ± 0.8	0.89
			2	5–8	15–20	−2.3 ± 0.5	216 ± 18	3.8 ± 0.8	0.88
			4	5–12	10–20	−3.4 ± 0.8	180 ± 11	5.5 ± 0.6	0.93
			4	5–8	15–25	−2.3 ± 0.7	205 ± 19	3.8 ± 0.9	0.89
			2	9–15	10–15	−3.4 ± 0.6	220 ± 10	5.6 ± 0.5	0.89
			3	9–18	20–25	−3.0 ± 0.8	218 ± 10	5.0 ± 0.7	0.88
			4	7–30	20–30	−3.1 ± 0.5	209 ± 9	5.0 ± 0.7	0.89
			4	5–10	15–25	−2.3 ± 0.7	285 ± 5	3.8 ± 0.6	0.78
			4	5–20	10–15	−4.0 ± 0.5	204 ± 17	6.4 ± 0.4	0.91
			1	5–10	20	−1.8	205	3.1	0.88
			2	10–45	20–25	−2.1 ± 0.5	225 ± 10	3.5 ± 0.3	0.86
			3	5–35	20–30	−2.5 ± 0.7	215 ± 15	4.2 ± 0.6	0.88
			4	10–30	15–25	−2.0 ± 0.5	212 ± 10	3.3 ± 0.8	0.88
			3	12–30	20–25	−3.1 ± 0.8	213 ± 9	5.1 ± 0.7	0.89
			4	5–12	10–20	−3.0 ± 0.8	209 ± 15	5.0 ± 0.9	0.89
			2	8–10	10–15	−3.3 ± 0.6	210 ± 13	5.4 ± 0.8	0.90
			3	8–30	15–25	−2.2 ± 0.8	214 ± 10	3.7 ± 0.5	0.88
		Sphalerite	3	5–8	20–25	−2.0 ± 0.5	214 ± 10	3.3 ± 0.8	0.88
			5	5–15	10–20	−2.0 ± 0.7	214 ± 8	3.4 ± 0.9	0.88
			4	10–18	20–30	−1.8 ± 0.5	217 ± 11	3.1 ± 0.6	0.87
			2	5–35	20–25	−2.7 ± 0.4	200 ± 13	4.4 ± 0.8	0.90
			3	15–25	10–15	−3.3 ± 0.5	195 ± 11	5.5 ± 0.4	0.91
			2	8–10	15–25	−3.3 ± 0.6	203 ± 15	5.3 ± 0.8	0.90
			2	15–50	10–20	−3.6 ± 0.3	249 ± 9	5.8 ± 0.5	0.85
			3	12–18	20–25	−3.5 ± 0.6	239 ± 10	5.7 ± 0.8	0.87
			3	5–18	15–25	−3.3 ± 0.5	191 ± 15	5.4 ± 0.6	0.92
			3	10–15	10–15	−2.5 ± 0.7	184 ± 10	4.1 ± 0.5	0.91
			4	10–40	20–30	−3.2 ± 0.5	170 ± 17	5.3 ± 0.7	0.94
			4	5–15	10–20	−3.3 ± 0.4	189 ± 9	5.4 ± 0.5	0.92
			3	5–20	10–15	−2.0 ± 0.5	188 ± 10	3.4 ± 0.8	0.90
			5	10–15	15–25	−3.3 ± 0.7	204 ± 12	5.4 ± 0.9	0.90
			1	15	25	−3.6 ± 0.5	242 ± 10	5.9 ± 0.4	0.86
			3	10–20	20–25	−2.1 ± 0.8	208 ± 12	3.6 ± 0.8	0.88
	Quartz-calcite-manganese oxides-hydroxides stage (ore-stage 3)								
		Quartz	2	8–10	10–15	−0.3 ± 0.6	163 ± 9	0.4 ± 0.3	0.91
			5	5–15	15–25	−0.4 ± 0.5	194 ± 5	0.7 ± 0.8	0.88

(Continued on following page)

TABLE 2 (*Continued*) Microthermometric data for primary type 1 fluid inclusion assemblages from Tashvir and Varmazyar deposits.

		Host mineral	n	Size (μm)	Vapor (vol%)	$T_{m\text{-}ice}$ (°C)	T_h (°C)	Salinity (wt.% NaCl equivalent)	ρ (g/cm^3)
			5	5–10	10–20	−1.2 ± 0.8	173 ± 10	2.1 ± 0.6	0.91
			4	5–20	15–25	−0.5 ± 0.5	169 ± 15	0.9 ± 0.8	0.91
			4	8–12	10–20	−0.5 ± 0.4	171 ± 12	0.9 ± 0.5	0.90
			3	5–18	20–25	−0.1 ± 0.8	165 ± 10	0.2 ± 0.7	0.90
			3	5–10	10–20	−1.5 ± 0.5	153 ± 11	2.6 ± 0.4	0.93
			3	8–10	10–15	−0.5 ± 0.8	175 ± 8	0.9 ± 0.5	0.90
			3	5–10	15–25	−0.7 ± 0.6	185 ± 10	1.2 ± 0.9	0.89
			5	5–20	20–25	−0.3 ± 0.7	180 ± 12	0.5 ± 0.7	0.89
			4	5–15	15–25	−1.5 ± 0.8	124 ± 15	2.5 ± 0.8	0.91

n: Number of FIs measured in individual FIAs.
The few homogenization temperatures for type 2 inclusions are not listed here but are described in the text.
$T_{m\text{-}ice}$ = final melting temperatures of ice, T_h = homogenization temperature.

zircon U–Pb dating for the emplacement of the intrusions at THMB (~40–36 Ma; Nabatian et al., 2014; Nabatian et al., 2016; Aghazadeh et al., 2015; Kouhestani, 2018; Mokhtari et al., 2022a).

4.2 Fluid inclusion petrography

Based on detailed FI petrography, three different types of FIs recognized at both the Tashvir and Varmazyar deposits (Figure 9): 1) liquid-rich two-phase aqueous inclusions (type 1), 2) vapor-rich two-phase aqueous inclusions (type 2), and 3) monophase vapor inclusions (type 3). There are also some monophase liquid inclusions in some samples that are probably the results of decrepitation or necking-down. Type 1 inclusions are the most abundant, >85 vol.% of the total FI populations, and are widespread in both quartz and sphalerite grains. These FIs contain liquid (70–90 vol.%) and vapor (10–30 vol.%) phases at room temperature and are primarily negative-crystal shaped, rounded, irregular, or elliptical with sizes between 5 and 50 μm (Figures 9A–F). They have no daughter minerals and are homogenized to the liquid phase. Type 2 inclusions contain vapor volumetric proportions around 50 to near 80%. These FIs are less abundant and mostly occur isolated or coexist with type 1 inclusions (Figures 9A, C–E). They vary in size from 5 to 30 μm, show negative crystal, irregular or ellipse shapes, and are homogenized to vapor when heated. Type 3 inclusions comprise only a vapor phase at room temperature (Figures 9A, C–E). They mainly appear as isolated, randomly distributed, and vary in size from <5 to 20 μm. No inclusions contained visible liquid CO_2. Although all three types of FIs found in the same quartz and sphalerite crystals, most FIs in quartz from ore-stage 1 at Tashvir and quartz and sphalerite from ore-stage 2 at Varmazyar were types 1 and 2 inclusions. Inclusions within quartz from the ore-stage 2 at Tashvir and ore-stage 3 at Varmazyar were commonly type 1.

4.3 Microthermometric results

Only FIs thought to be primary (e.g., occur as isolations, and in clusters, Roedder, 1984; Goldstein, 2003) are selected for microthermometry. FIAs are defined as clusters or groups of inclusions that have similar phase proportions at room temperature (e.g., Goldstein and Reynolds, 1994). The mean values of individual FIAs, rather than those of individual FIs, are used to avoid data bias. Pseudo-secondary (occur as clusters and trails that are truncated at crystal boundaries), and secondary (distributed in trails crosscutting crystal boundaries) inclusions were not measured. The microthermometric results are summarized in Table 2.

4.3.1 Tashvir deposit

At Tashvir, microthermometric measurements were performed on primary type 1 FIAs hosted by quartz in ore-stages 1 and 2. The two-phase aqueous type 1 inclusions at the Tashvir deposit have bulk densities of 0.80–0.94 g/cm^3 (Table 2). Quartz-hosted type 1 inclusions in FIAs of ore-stage 1 had the final melting temperatures of ice ($T_{m\text{-}ice}$) from −5.0 to −1.5°C, which corresponds to calculated salinities of 2.6–7.9 (average value of 4.9) wt.% NaCl equivalent. They have homogenization temperatures

(T_h) range from 186 to 287°C, with an average value of 224°C. Clustered FIs within quartz from ore-stage 2 yielded $T_{m\text{-}ice}$ varying from −1.3 to −0.3°C (Table 2). The calculated salinities range from 0.5 to 2.7 (average value of 1.5) wt.% NaCl equivalent. These inclusions have T_h from 130 to 182°C, with the average value at 162°C. The T_h values of type 2 inclusions with small amounts of liquid contents could not normally be determined. Only five homogenization temperatures of type 2 FIs in quartz from ore-stage 1 were measured. They homogenize at temperatures ranging from 190 to 270°C, which is comparable with those of neighboring type 1 inclusions. It is hard to measure the $T_{m\text{-}ice}$ values of type 2 FIs, due to small amounts of liquid contents.

4.3.2 Varmazyar deposit

In the Varmazyar deposit, we analyzed primary type 1 FIAs hosted by quartz and honey-colored (Fe-poor) sphalerite in ore-stages 2 and 3. Type 1 inclusions in quartz from ore-stage 2 have $T_{m\text{-}ice}$ vary from −4.0 to −1.8°C, corresponding to the salinities of 3.1–6.4 (average value of 4.5) wt.% NaCl equivalent. These inclusions homogenized at temperatures ranging from 180 to 285 °C, with the average value at 214 °C. They have calculated bulk density of 0.78–0.93 g/cm^3. Sphalerite-hosted type 1 inclusions in FIAs of ore-stage 2 record $T_{m\text{-}ice}$ values ranging from −3.6 to −1.8°C with corresponding salinity ranges from 3.1 to 5.9 (average value of 4.7) wt.% NaCl equivalent. These fluids homogenized at temperatures between 170 and 249 °C, with the average value at 207 °C and densities ranging from 0.85 to 0.94 g/cm^3 (Table 2). In the ore-stage 2, both quartz- and sphalerite-hosted type 2 inclusions showed meaningly different vapor/liquid ratios and had highly variable T_h values. Few of these inclusions in discrete FIAs homogenized to the vapor phase with the T_h values of 200–255°C within quartz and 180–225°C within sphalerite, which is parallel with those of type 1 inclusions in close areas. It is difficult to observe the final ice melting for type 2 inclusions in quartz and sphalerite (e.g., Roedder, 1984; Bodnar et al., 1985); therefore, we did not obtain any $T_{m\text{-}ice}$ values of these FIs. The $T_{m\text{-}ice}$ values of quartz-hosted type 1 inclusions in FIAs of ore-stage 3 are −1.5 to −0.1°C, yielding salinities of 0.2–2.6 (average value of 1.2) wt.% NaCl equivalent. FIs within quartz of ore-stage 3 homogenize at temperatures between 124 and 194°C, with an average value at 168 °C, and a density range of 0.88–0.93 g/cm^3.

4.4 O–S isotopic compositions

Oxygen and sulfur isotope data from the Tashvir and Varmazyar deposits are listed in Table 3. The $\delta^{18}O_{VSMOW}$ values of quartz samples in ore-stages 1 and 2 at Tashvir are +10.2‰ and +7.9‰, respectively (Table 3). These values for quartz samples of ore-stages 2 and 3 at Varmazyar are +9.7 to +9.3‰ and +8.9‰, respectively (Table 3). The calculated $\delta^{18}O_{water\text{-}VSMOW}$ values of the ore-forming fluids range from +4.2‰ to +0.9‰ at Tashvir and +4.3‰ to +1.4‰ at Varmazyar (Table 3). Two calcite samples from ore-stage 3 at Tashvir and ore-stage 4 at Varmazyar yield $\delta^{18}O_{VSMOW}$ values of +15.3‰ and +14.1‰, respectively. Using the calcite–water fractionation equation of Zheng (1999) and the average homogenization temperatures of FIAs, the $\delta^{18}O_{water\text{-}VSMOW}$ values of the ore-forming fluids are calculated to be −0.5‰ and −1.7‰, respectively (Table 3).

The six galena, chalcopyrite, and chalcocite samples from the early quartz-sulfide ore-stage at Tashvir yield $\delta^{34}S_{CDT}$ values of −20.2‰ to −7.9‰ (average −14.4‰) and the six galena and sphalerite samples from the second quartz–sulfide ore-stage at Varmazyar yield $\delta^{34}S_{CDT}$ values of −9.1‰ to −6.5‰ (average −7.8‰) (Table 3). The calculated $\delta^{34}S_{H2S\text{-}CDT}$ values range from −17.8‰ to −5.1‰ (average −12.7‰) at Tashvir and −8.6‰ to −3.8‰ (average −6.1‰) at Varmazyar (Table 3).

5 Discussion

5.1 Timing of epithermal base metal mineralization

In the past decade, many precious and base metal epithermal deposits have been found in the THMB, forming it as one of the most significant metallogenic belts in northwestern Iran. These deposits occur as quartz-sulfide veins in the fissures of the Eocene (zircon U–Pb ages of 49.3 ± 2.9 to 41.1 ± 1.6 Ma, Verdel et al., 2011) volcanic-volcaniclastic strata of the Karaj Formation, and hydrothermal alterations (i.e., silicification, intermediate argillic, chloritization, carbonatization, and propylitic) can be found in the ore-bearing volcanic-volcaniclastic strata. These alterations, together with the ore veins, are mainly controlled by fault structures, indicating that they should have formed later than their Eocene volcanic-volcaniclastic host rocks (e.g., Heald et al., 1987; John et al., 2003; Henning et al., 2008; Kirk et al., 2014; Peng et al., 2021). The geological investigations revealed that almost all the epithermal deposits in the THMB clustered around the late Eocene (~40–36 Ma, Nabatian et al., 2014; Nabatian et al., 2016; Aghazadeh et al., 2015; Kouhestani, 2018; Mokhtari et al., 2022a) granitoid intrusions (Figure 1). There is now a broad consensus that these deposits resulted from shallow magmatic-hydrothermal processes related to the late Eocene magmatism (e.g., Ghasemi Siani et al., 2015; Mehrabi et al., 2016; Kouhestani et al., 2018a; 2019a; b, 2020, 2022). Mehrabi et al. (2016) reported a biotite Ar-Ar age of 41.87 ± 0.16 Ma for the crystallization of the Goljin granite intrusion, which was considered closely related to the Au mineralization of the Gulojeh deposit. This age approximately overlaps with the sericite Ar-Ar isochron age of 42.20 ± 0.34 Ma for the hydrothermal alteration and gold mineralization event in the Gulojeh deposit (Ghasemi Siani et al., 2015). Accordingly, it was suggested there is a close spatial-temporal and genetic relationship between the Gulojeh

TABLE 3 Sulfur and oxygen isotope data for the Tashvir and Varmazyar deposits.

Deposit	Sample no.	Stages of mineralisation	Mineral	$\delta^{34}S$ ‰ CDT	$\delta^{34}S_{H2S}$[a]‰ CDT	
Tashvir	T-01	ore-stage 1	Galena	−20.2	−17.8	
	T-02	ore-stage 1	Galena	−18.1	−15.7	
	T-03	ore-stage 1	Chalcopyrite	−13.0	−13.2	
	T-04	ore-stage 1	Chalcopyrite	−15.6	−15.8	
	T-05	ore-stage 1	Chalcocite	−11.5	−8.7	
	T-06	ore-stage 1	Chalcocite	−7.9	−5.1	
Varmazyar	V-01	ore-stage 2	Galena	−9.1	−6.4	
	V-02	ore-stage 2	Galena	−6.5	−3.8	
	V-03	ore-stage 2	Galena	−8.0	−5.3	
	V-04	ore-stage 2	Galena	−6.9	−4.2	
	V-05	ore-stage 2	Sphalerite	−8.2	−8.6	
	V-06	ore-stage 2	Sphalerite	−8.1	−8.5	
					$\delta^{18}O$‰ VSMOW	$\delta^{18}O_{water}$[b]‰ VSMOW
Tashvir	T-07	ore-stage 1	Quartz		10.2	4.2
	T-08	ore-stage 2	Quartz		7.9	0.9
	T-09	ore-stage 3	Calcite		15.3	−0.5
Varmazyar	V-07	ore-stage 2	Quartz		9.7	4.3
	V-08	ore-stage 2	Quartz		9.3	4.1
	V-09	ore-stage 3	Quartz		8.9	1.4
	V-10	ore-stage 4	Calcite		14.1	−1.7

[a]$\delta^{34}S_{H2S}$ values were calculated using the fractionation equation of Li and Liu (2006).
[b]$\delta^{18}O_{water}$ values in quartz and calcite were calculated using the fractionation equation of Matsuhisa et al. (1979) and Zheng (1999), respectively.
Average homogenization temperatures of FIAs (Table 1) were used to calculate isotope values.

Au mineralization and Goljin granite intrusion (Ghasemi Siani et al., 2015; Mehrabi et al., 2016). In the case of the Tashvir and Varmazyar deposits, the mineralized quartz veins have crosscutting relationships with their Eocene volcanic-volcaniclastic host rocks. In both deposits, granitoid intrusions intruded into the Eocene volcanic-volcaniclastic strata and have, especially at Varmazyar, close spatial relationships with epithermal base metal mineralization. By analogy to the age of Au mineralization in the neighboring Gulojeh deposit and assuming that magmatic-related ore-forming fluids are responsible for the epithermal mineralization in the THMB, we speculate that zircon U–Pb crystallization ages of granitoid intrusions, 38.34–38.31 and 40.85 Ma (Table 1; Figure 8), might mirror the age of epithermal mineralization in the Tashvir and Varmazyar deposits. However, more attention is needed to be paid to illustrating the spatial patterns of the epithermal mineralization and granitoid intrusions, and detailed geochronological frameworks should be integrated with systematic geological observation to obtain the exact timing of the epithermal mineralization. The late Eocene is not only a primary period of plutonism but also an essential stage of large-scale epithermal mineralization in the THMB. This model can provide an essential guide for regional epithermal precious and base metal exploration in the THMB.

5.2 Source of ore-forming fluids

It has been discussed that the fluids responsible for HS mineralization are mostly highly acidic and oxidized magmatic fluids that interacted with much lesser amounts of meteoric water (Hedenquist et al., 1998, 2000; Qin and Ishihara, 1998; Einaudi et al., 2003; Sillitoe and Hedenquist, 2003; Simmons et al., 2005; Henley and Berger, 2011). In contrast, LS deposits are derived from reduced, near-neutral pH, and dilute fluids formed by the entrainment of magmatic components within deep circulating meteoric waters (White and Hedenquist, 1990; Hedenquist and Lowenstern, 1994;

10.3389/feart.2022.990761

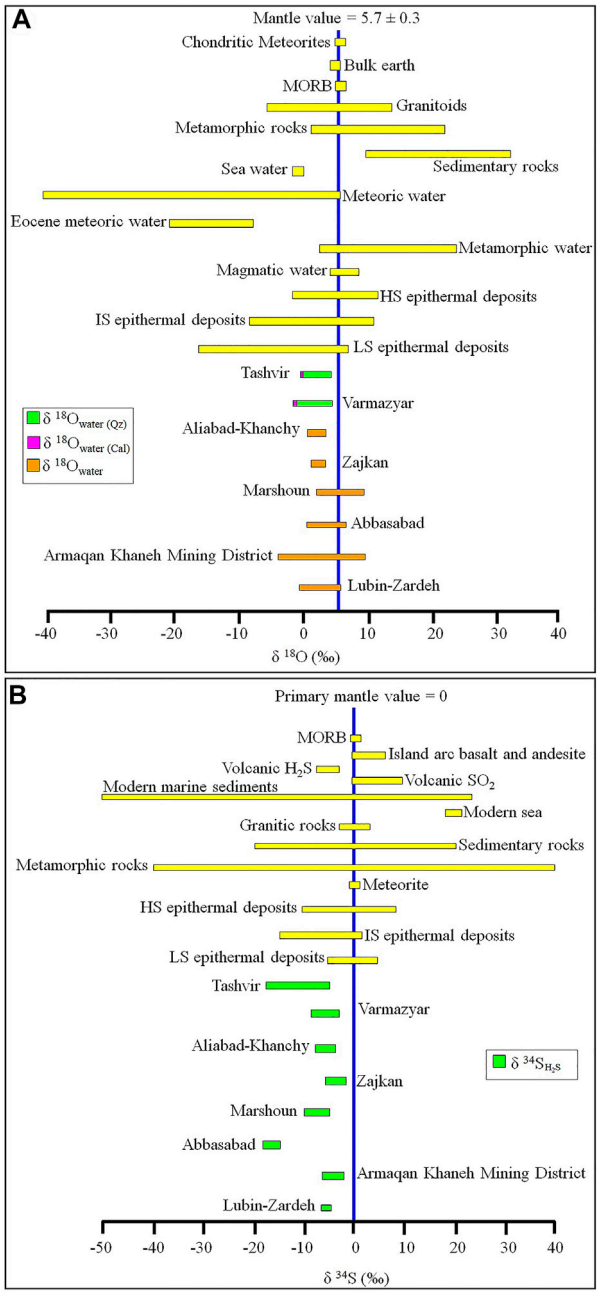

FIGURE 10
Comparison of oxygen **(A)** and sulfur **(B)** isotope compositions of the Tashvir and Varmazyar deposits (this study) with those from important geological reservoirs (Hoefs, 2018), typical high-, intermediate- and low-sulfidation epithermal deposits (Field and Fifarek, 1985; Hedenquist and Lowenstern, 1994; Arribas, 1995; Albinson et al., 2001; Oyman, 2019; Sun et al., 2021 and references therein) and major intermediate-sulfidation epithermal base metal deposits of the THMB (Kouhestani et al., 2018a; 2019a; b, 2020, 2022; Zamanian et al., 2019).

Matsuhisa and Aoki, 1994; White et al., 1995; Cooke and Simmons, 2000; Hedenquist et al., 2000; Simmons et al., 2005). IS deposits form from reduced, and near-neutral pH hydrothermal fluids similar to LS deposits, nevertheless they have direct links with magmas and show strong magmatic signatures in their mineralizing fluids (Gemmell, 2004; Kouhestani et al., 2015; Mehrabi et al., 2016; Xie et al., 2017; Li et al., 2018).

The ore-forming fluids associated with quartz and calcite from different ore-stages at Tashvir and Varmazyar have $\delta^{18}O_{water\text{-}VSMOW}$ values ranging from +4.2‰ to −0.5‰ and +4.3‰ to −1.7‰, respectively (Table 3). These data are similar to the oxygen isotope data of global epithermal systems and IS epithermal base metal deposits of the THMB (Figure 10A). Considering the geological setting in which formed the Tashvir and Varmazyar hydrothermal systems, the $\delta^{18}O_{water\text{-}VSMOW}$ values of earlier quartz samples (+4.2‰ and +4.3‰) are nearly close to the $\delta^{18}O$ values of magmatic source (5.5‰–10‰; Taylor, 1974; Sheppard, 1986; Hoefs, 2018). The lower $\delta^{18}O_{water\text{-}VSMOW}$ values of the calcite samples from the later ore-stages (−0.5‰ and −1.7‰) are closer to the $\delta^{18}O$ values of Eocene meteoric water (−21‰ to −8‰; Koch et al., 1995; Seal and Rye, 1993). This advises that the initial fluids may be magmatic but mixed with meteoric water during the later stages of ore formation, which is usual in other global epithermal ore systems (e.g., Tindell et al., 2018; Guimarães et al., 2021; He et al., 2021; Peng et al., 2021; Xu et al., 2021; Figueroa et al., 2022; Niu and Jiang, 2022). Such interpretation is further supported by FIs evidence for fluid mixing of magmatic and meteoric fluids during the mineralizing event. In both the Tashvir and Varmazyar deposits, microthermometry results suggested that the ore-forming fluids in the early ore-stages belong to an H_2O-NaCl system with temperatures of 224 and 214–207°C and salinities of 4.9 and 4.5–4.7 wt.% NaCl equivalent, which is consistent with those from magmatic-hydrothermal fluids (Burnham, 1979; Hedenquist and Lowenstern, 1994; Baker, 2002; Simmons and Brown, 2006; Audétat et al., 2008). In the late ore-stages, the FIs are characterized by temperatures of 162 and 168°C and salinities of 1.5 and 1.2 wt.% NaCl equivalent, likely reflecting the dominant involvement of meteoric water in accordance with the oxygen isotope data.

A similar scenario has been documented for several epithermal deposits within the THMB, including Aliabad-Khanchy, Zajkan, Marshoun, Abbasabad, Rashtabad, Jalilabad, Aqkand, and Lubin-Zardeh. These deposits have $\delta^{18}O_{water}$ values ranging from +9.6‰ to −3.4‰ (Kouhestani et al., 2018a; 2019a; b, 2020, 2022; Zamanian et al., 2019), suggesting that their ore-forming fluids were most likely magmatic-derived in the early stages, but were mixed with meteoric water in the late stages. It is consistent with the geological characteristics of these deposits that are indicative of an IS epithermal origin for these deposits.

5.3 Ore-forming material and sulfur sources

Sulfur isotope systematic provides a valuable tool for outlining the sources of sulfur and ore-forming components in mineral deposits (Ohmoto, 1972, 1986; Ohmoto and Goldhaber, 1997; Seal, 2006; Lei et al., 2018). In the hydrothermal systems, sulfur isotope compositions of sulfides depend on the total sulfur values of source materials and physicochemical conditions (i.e., sulfur and oxygen fugacity, pH, and temperature variations) of ore-forming fluids (Ohmoto and Rye, 1979; Williams-Jones and Migdisov, 2014; Hoefs, 2018; Lei et al., 2018). In the Tashvir and Varmazyar deposits, sulfide assemblages are simple, and sulfate minerals are absent, demonstrating weak sulfur fractionation and a reduced mineralization environment. Thus, the sulfur isotope composition of sulfides could approximately represent the total sulfur values of ore-fluids (Ohmoto and Rye, 1979; Ohmoto and Goldhaber, 1997; Li et al., 2012; Sun et al., 2021; Yu et al., 2021; Zhao et al., 2021; Yang et al., 2022).

Sulfide minerals from the Tashvir deposit show a wide range of $\delta^{34}S_{H2S\text{-}CDT}$ values from −17.8‰ to −5.1‰ (average −12.7‰), and those from the Varmazyar deposit fall into a narrow range from −8.6‰ to −3.8‰, averaging −6.1‰. These data are lower than the range of mantle/magmatic $\delta^{34}S_{VCDT}$ values (±3‰; Chaussidon and Lorand, 1990) and are similar to the sulfur isotope compositions of IS epithermal base metal deposits (e.g., Aliabad-Khanchy, Zajkan, Marshoun, Abbasabad, Armaqan Khaneh, and Lubin-Zardeh) in the THMB (Figure 10B), whose sulfur is interpreted to have been originated from the magmatic system (Kouhestani et al., 2018a; Kouhestani et al., 2019a; Kouhestani et al., 2019b; Zamanian et al., 2019; Kouhestani et al., 2020; Kouhestani et al., 2022). Compared with different types of epithermal systems, $\delta^{34}S$ values of the Tashvir and Varmazyar deposits are mostly consistent with the HS and IS deposits (Figure 10B). In addition, the sulfur isotopic values of the Tashvir and Varmazyar deposits overlap with those of reduced sulfur in sedimentary rocks ($\delta^{34}S$ = <−15‰; Rollinson, 1993) and volcanic H_2S. These more negative $\delta^{34}S_{H2S\text{-}CDT}$ values can be interpreted as a result of oxygen fugacity changes or mixing between igneous and sedimentary sulfur (Ohmoto, 1972; Pearson et al., 1988; Pass et al., 2014; Liu et al., 2017; Lei et al., 2018). There is no evidence indicating the occurrence of fO_2 changes in the quartz-sulfide ore-stages of the Tashvir and Varmazyar deposits. Moreover, Mousavi Motlagh et al. (2019) reported the existence of framboidal pyrite in the host volcaniclastic rocks ($\delta^{34}S$ = −5.3‰ to −7.3‰) of the Chargar deposit which they suggested as the primary sedimentary source for sulfur. Thus, we conclude that $\delta^{34}S_{H2S\text{-}CDT}$ signatures of the Tashvir and Varmazyar deposits should specify the mixture of magmatic-derived and sedimentary-sourced sulfur (e.g., Hoefs, 2018; Mousavi Motlagh et al., 2019; Liu et al., 2021; Sun et al., 2021). The sedimentary pyrite sulfur source is expected to be derived from fluid-rock reactions between magmatic-sourced fluids and volcanic-volcaniclastic rocks of the Karaj Formation.

5.4 Minimum fluid trapping pressure and mineralization depth

An independent P or T constrain is needed for real trapping conditions estimations except for the boiling assemblage (i.e., coexisting brine polyphase and vapor FIs) which thought its temperature and pressure of homogenization represents actual fluid entrapment condition (e.g., Roedder and Bodnar, 1980; Simmons et al., 2005; Rusk et al., 2008; Kouhestani et al., 2015, 2020; Rabiei et al., 2017; Zhai et al., 2018; Sun et al., 2021). It is important to note that there was no evidence of boiling in the samples studied during our FI analysis. Consequently, the estimation of the minimum trapping pressure was calculated with the sowatflinc_inclusion computer program (Driesner and Heinrich, 2007) assuming the H_2O-NaCl system. The results show that quartz-sulfide veins of ore-stage 1 at Tashvir have minimum hydrostatic pressures varying from 11 to 69 (average 26) bars, and those for ore-stage 2 quartz veins range from 3 to 10 (average 7) bars. The calculated minimum trapping pressures for quartz-sulfide veins of ore-stage 2 at Varmazyar range from 8 to 68 (average 20) bars, and those for ore-stage 3 quartz veins vary from 2 to 14 (average 8) bars. Based on these data and related trapping pressure estimations, we conclude that ore-stage quartz-sulfide veins at Tashvir and Varmazyar essentially occurred at minimum hydrostatic pressures of 10–69 and 14–68 bars, respectively. Taking the average density of the FIs, the inferred minimum metallogenic paleodepths range from 103 to 706 m at Tashvir and 143–695 m at Varmazyar, which are comparable with those of mineralization depth of the epithermal deposits worldwide (<300–1,000 m, Cooke and Simmons, 2000; Albinson et al., 2001; Simmons et al., 2005), e.g., in the THMB of northwestern Iran (200–1,400 m, Kouhestani et al., 2018a; 2019a; b, 2020, 2022; Zamanian et al., 2019).

5.5 Fluid evolution and mineralization mechanism

Previous works revealed that boiling, dilution, and cooling or a combination of them are key fluid processes that enhance ore formation in the magmatic-hydrothermal systems (e.g., Hedenquist and Henley, 1985; Wilkinson, 2001; Canet et al., 2011). FI microthermometric measurements from the Tashvir and Varmazyar deposits show that ore-forming fluids belong to the H_2O–NaCl systems that evolved from a high-to moderate-temperature and moderate-salinity fluid to a low-temperature and low-salinity fluid during the mineralization processes. This decrease in temperature and salinity is consistent with the

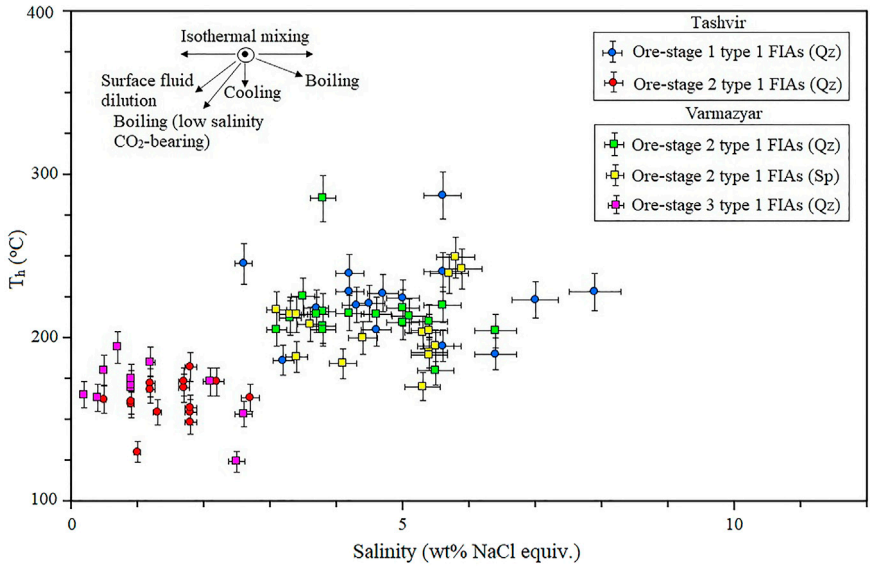

FIGURE 11
T_h-salinity plot showing the evolution of FIs representing ore-forming fluids for different ore-stages at the Tashvir and Varmazyar deposits. Inset illustrates the different fluid evolution paths based on Wilkinson (2001).

cooling and dilution of magmatic fluids that are mixed with meteoric waters (e.g., Hedenquist and Henley, 1985; Wilkinson, 2001; Kouhestani et al., 2015, 2020; Zhao et al., 2021; Niu and Jiang, 2022; Shi et al., 2022). This is in agreement with oxygen isotopic data, which shows that hydrothermal fluids at Tashvir and Varmazyar are magmatic-meteoric mixtures. On the fluid evolution diagram (Figure 11), the inclusions of the Tashvir and Varmazyar deposits show two groups of salinities with a positive T_h vs salinity correlation, reflecting that mineralization at these deposits involved the mixing of magmatic fluids and a dilute, cooler fluid of meteoric origin (e.g., Ulrich et al., 2001; Zhai et al., 2009; Canet et al., 2011; Li et al., 2019; Kouhestani et al., 2015; 2019a; b, 2020, 2022; Sun et al., 2021).

It has been discussed that silver and base metals (Pb, Zn, and Cu) are commonly transported as chloride complexes in hydrothermal fluids (e.g., Stefansson and Seward, 2003; Yardley, 2005). Fluid mixing can significantly alter the phase equilibrium of the hydrothermal fluid that cause the breakup of the chloride complexes and led to the precipitation of metal sulfides (Kouhestani et al., 2015; 2019a; b, 2020; An and Zhu, 2018; Wang L. et al., 2019). Therefore, fluid mixing is the main mechanism that could explain the deposition of base metal sulfides in mineralized ore veins at Tashvir and Varmazyar. Nevertheless, in both deposits, the presence of bladed calcite (later replaced by quartz), as well as plumose and colloform/crustiform banded quartz indicate that boiling also occurred during the evolution of the Tashvir and Varmazyar hydrothermal systems (e.g., White and Hedenquist, 1990; Hedenquist et al., 2000; Moncada et al., 2012, 2017; Kouhestani et al., 2019a; b, 2020, 2022). This is further supported by the occurrence of hydrothermal breccias in ore-stage veins, which is evidence of sharp pressure drops that might have caused fluid boiling (e.g., Jobson et al., 1994; Jébrak, 1997). It has been argued that at relatively shallow levels, fluid boiling can increase the permeability of host rocks allowing meteoric water influx into the hydrothermal system (e.g., Zhai et al., 2018) which generally causes temperature decreases, allowing base metals deposition (e.g., Henley, 1985; Fan et al., 2011; Zhong et al., 2018). An increase in pH that accompanied boiling also enhanced base metal precipitation (e.g., Thiersch et al., 1997).

5.6 Mineralization type

Compared to typical characteristics of epithermal deposits (Table 4), the geological and mineralogical features of the Tashvir and Varmazyar deposits are similar to those of IS epithermal deposits. In both deposits, orebodies consist of brecciated veins and veinlets and are hosted by fault-controlled alteration zones. The absence of Mn carbonates and sulfosalt minerals set the Tashvir and Varmazyar deposits apart from the IS epithermal deposits. However, their sulfide assemblages of pyrite, chalcopyrite, galena, sphalerite, and local chalcocite and bornite suggest an IS state (e.g., Hedenquist et al., 2000; Sillitoe and Hedenquist, 2003; Simmons et al., 2005; Camprubi and Albinson, 2007; Wang X. et al., 2019; Peng et al., 2021). The lack of adularia along with

TABLE 4 Comparison of main characteristics of the Tashvir and Varmazyar deposits with different types of epithermal deposits (Cooke and Simmons, 2000; Hedenquist et al., 2000; Einaudi et al., 2003; Sillitoe and Hedenquist, 2003; Simmons et al., 2005).

	Epithermal deposits				
	HS	IS	LS	Tashvir	Varmazyar
Depth of formation	<500–1,000 m	300–800 m, rarely >1,000 m	<300 m	103–716 m	123–665 m
Typical host rocks	Lava flows and pyroclastic units, diatremes, porphyries	Lava flows, pyroclastic, basement, diatremes	Domes, volcaniclastic and sedimentary units	Volcanic and volcaniclastic units	Volcanic and volcaniclastic units
Deposit style	Replacement, dissemination, breccia bodies, massive veins	Veins, vein breccia, breccia infill, stockwork, dissemination	Veins, stockwork, vein breccia, breccia infill, dissemination	Veins, vein breccia, stockwork, breccia infill, dissemination	Veins, vein breccia, breccia infill, dissemination
Key ore minerals	Py, Eng, Lzn,Fmt, Cv, Dg	Py, Sp (Fe-poor),Gn, Ttr, Tnt, Ccp	Py, Mrc, Apy, Prg, Acn (minor Fe-rich Sp, Ccp, Po)	Ccp, Cct, Gn, Sp (lesser Bn)	Gn, Sp (Fe-poor), Py, Ps, Pyr
Gangue minerals	Qz, Alu, Brt, Kln, Anh, Dck, Prl	Qz, Clc, Cal ±Mn Cb, Adl, Brt, Mn Silicate	Qz, Clc, Cal, Adl, Ilt, Chl, minor Fl	Qz, Clc, Cal, Chl	Qz, Clc, Cal
Mineral textures	Vuggy Qz, massive sulfide, late veins/breccias, replacement	Crustiform, colloform, cockade, comb, carbonate replacement	Crustiform, colloform, cockade, comb, carbonate replacement	Veins/breccias, vug infill, colloform, crustiform, plumose	Veins/breccias, comb, colloform, crustiform, cockade, bladed calcite, plumose, vug infill
Proximal alteration mineralogy	Qz, Alu, Prl,Dck	Ser, quartz, Cb(Mn varieties common)	Ilt/Sme, Adl, Cb (non-manganiferous)	Qz, Ser–Ilt, Cb, Chl	Qz, Ser–Ilt, Cb
Metal signature	Au-Ag, Cu, As-Sb	Ag-Au, Zn, Pb, Cu	Au ± Ag	Pb–Zn (Cu, Ag)	Pb–Zn (Ag)
Sulfidation state indicators	Eng, Lzn, Fmt	Ttr, Ccp, Sp (Fe-poor)	Po, Apy, Sp (Fe-rich)	Ccp, Gn, Sp (Fe-poor)	Gn, Sp (Fe-poor)
Temperature and salinity	180–320 °C, <5 to 10 wt.% NaCl equivalent	200–300 °C, 0–23 wt.% NaCl equivalent	150–300 °C,< 2 wt.% NaCl equivalent	182–287 °C, 2.7–7.9 wt.% NaCl equivalent	194–285 °C, 2.6–6.4 wt.% NaCl equivalent
Fluid characteristics	Magmatic > meteoric, near-neutral, reduced	Magmatic-meteoric, near-neutral, reduced	Meteoric > magmatic, acidic, oxidized	Magmatic-meteoric, near-neutral, reduced	Magmatic-meteoric, near-neutral, reduced

Abbreviations: Acn: acanthite, Adl: adularia, Alu: alunite, Anh: anhydrite, Apy: arsenopyrite, Bn: bornite, Brt: barite, Cb: carbonate, Ccp: chalcopyrite, Cct: chalcocite, Chl: chlorite, Clc: chalcedony, Cv: covellite, Dck: dickite, Dg: digenite, Eng: enargite, Fl: fluorite, Fmt: famatinite, Gn: galena, Ilt: Illite, Kln: kaolinite, Lzn: luzonite, Mrc: marcasite, Po: pyrrhotite, Prg: pyrargite, Prl: pyrophyllite, Ps: psilomelane, Py: pyrite, Pyr: pyrolusite, Qz: quartz, Sme: smectite, Sp: sphalerite, Sr: sericite, Tnt: tennantite, Ttr: tetrahedrite. Abbreviations follow Whitney and Evans (2010).

the sulfide assemblages (pyrite, arsenopyrite, pyrrhotite) representing an LS state, as well as the vuggy quartz and primary advanced argillic alteration assemblages (alunite, kaolinite, pyrophyllite) and ore minerals (enargite and luzonite) of HS state differentiate Tashvir and Varmazyar from LS and HS epithermal deposits (e.g., White and Hedenquist, 1990, 1995; Cooke and Simmons, 2000; Hedenquist et al., 2000; Simmons et al., 2005; Wang L. et al., 2019). Additionally, the medium-to low-temperature alteration minerals (sericite, illite, epidote, calcite, and chlorite) and sulfide assemblages designate that epithermal mineralization at Tashvir and Varmazyar was formed by reduced and near-neutral pH ore-forming fluids that are signatures of IS deposits (e.g., Einaudi et al., 2003; Sillitoe and Hedenquist, 2003; Kouhestani et al., 2015; Wang X. et al., 2019; Soberano et al., 2021). As well, FIs studies show that temperature (182–287 and 194–285 °C) and salinity (2.7–7.9 and 2.6–6.4 wt.% NaCl equivalent) of the ore-forming fluids at these deposits are similar to the majority of IS epithermal deposits worldwide (e.g., Wang L. et al., 2019). The presence of hydrothermal breccia, colloform/crustiform banding, cockade, plumose, comb, and bladed calcite (later replaced by quartz), as well as open-space filling textures, and, particularly, the spatial and temporal association with volcanic and shallow granitoid intrusions specify that mineralization at Tashvir and Varmazyar occurred in shallow epithermal depth. The stable isotopic data indicate the mixing of magmatic and meteoric fluids as hydrothermal alteration proceeded, with some evidence of boiling. All these characteristics are similar to those of epithermal deposits of the IS-type, which are usually found in Phanerozoic volcano-plutonic settings (Wang X. et al., 2019; Guimarães et al., 2021), e.g., in the THMB of northwestern Iran (Kouhestani et al., 2017; 2018a; 2019a; b, 2020, 2022).

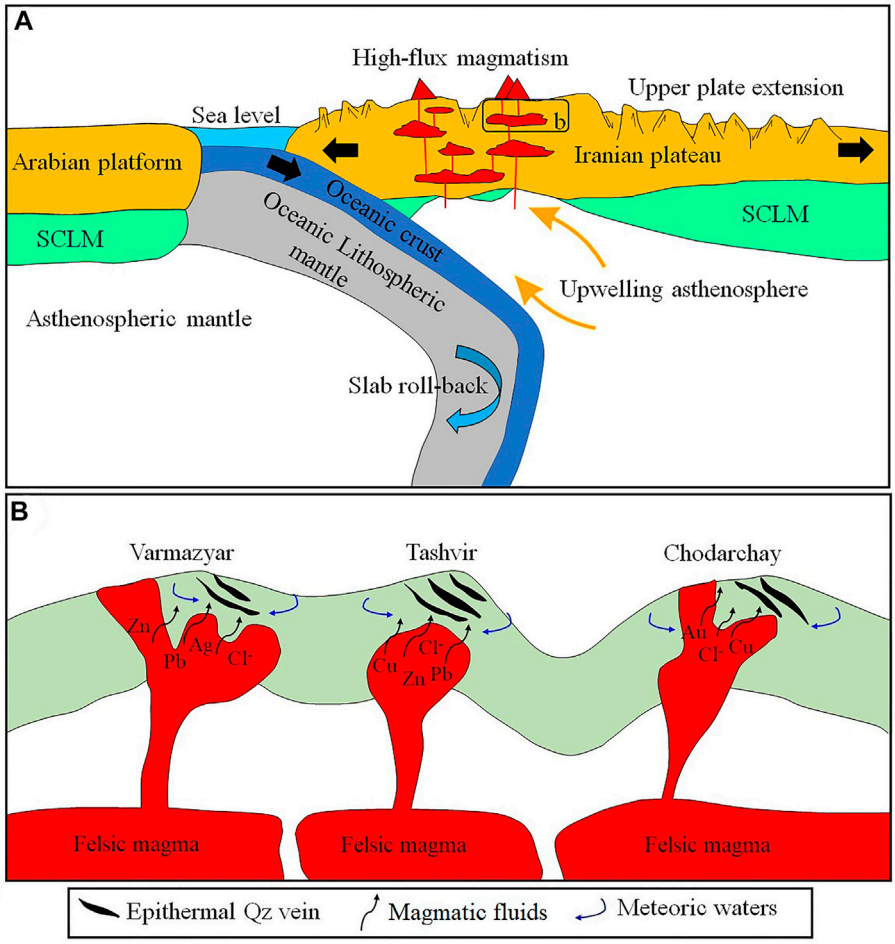

FIGURE 12
(A). Schematic cartoon for subduction, slab roll-back, extension, and magmatism in NW Iran (including THMB) during the Eocene time (based on Verdel et al., 2011; Shafaii Moghadam et al., 2018; Mokhtari et al., 2022b). **(B)**. Cartoon showing the type of fluids involved in the formation of the epithermal mineralization in the THMB.

5.7 Genetic model

The late Eocene granitoid intrusions in the THMB were intruded into the Eocene volcanic and volcaniclastic rocks of the Karaj Formation (Figure 1). They have close spatial associations with the epithermal quartz-sulfide veins, which suggest that the epithermal deposits in THMB may form related to these intrusions (e.g., Ghasemi Siani et al., 2015; Mehrabi et al., 2016; Kouhestani et al., 2018a; 2019a; b, 2020, 2022). Stable isotopic data from the Tashvir and Varmazyar deposits show evidence of genetic links between epithermal base metal mineralization and magmatism, representing that the metals, sulfur, and ore-forming fluid sources of these deposits are similar to global epithermal deposits (Cooke and Simmons, 2000; Hedenquist et al., 2000; Simmons et al., 2005; He et al., 2021), as well as other epithermal deposits in the THMB, including the Aliabad-Khanchy, Zajkan, Marshoun, Abbasabad, Rashtabad, Jalilabad, and Aqkand (Kouhestani et al., 2018a; 2019a; b, 2020, 2022). LA-ICP–MS zircon U–Pb dating demonstrates that granitoid intrusions from the Tashvir and Varmazyar crystallized at ca. 38.34–38.31 and 40.85 Ma, respectively (Figure 8), which mirrors the timing of ore formation. These ages are somehow similar to the age of the Gulojeh polymetallic deposit (42.20 ± 0.34 Ma, Ghasemi Siani et al., 2015; Mehrabi et al., 2016) in the THMB. These results indicate there happened large-scale magmatism and associated epithermal mineralization in the THMB in the late Eocene.

The Eocene flare-up magmatism in NW Iran (including THMB) is developed in the extensional environment caused by slab roll-back of the Neo-Tethyan oceanic crust (Verdel

et al., 2011; Shafaii Moghadam et al., 2018; Mokhtari et al., 2022b). A further response to the extension was the thinning of the thickened continental crust, asthenospheric upwelling, and partial melting of the subducting slab and metasomatized mantle wedge (Figure 12A, Agard et al., 2011; Verdel et al., 2011; Kargaran Bafghi and Neubauer, 2015; Shafaii Moghadam et al., 2018; Mokhtari et al., 2022b). This process led to the generation and emplacement of numerous late Eocene (37–42 Ma) granodiorite intrusions in the THMB (e.g., Aghazadeh et al., 2011; Castro et al., 2013; Nabatian et al., 2014, 2016; Kouhestani, 2018; Mokhtari et al., 2022a). It is generally accepted that these late Eocene intrusions contributed to the heat advection and composition of magmatic-hydrothermal fluids in the THMB (e.g., Ghasemi Siani et al., 2015; Mehrabi et al., 2016; Kouhestani et al., 2018a; 2019a; b, 2020, 2022; Ghasemi Siani et al., 2020). Some metallogenic elements and sulfur were transported well beyond the confines of the magmas by these fluids to shallower levels, where they mixed with meteoric waters, deposited and mineralized in syn-volcanic faults in the wall-rocks and the fissures formed through cooling of the intrusions (Figure 12B, Yasami et al., 2017; Kouhestani et al., 2018a; 2019a; b, 2020). Fluid cooling and/or dilution resulting from fluid mixing was likely the main promoting factor for base metal ore deposition.

In conclusion, the model proposed for the Tashvir and Varmazyar deposits highlights late Eocene syn-magmatic hydrothermal mineralization. This model also suggests that the close genetic relationship between late Eocene granitoid intrusions and epithermal mineralization in the THMB should form the basis for future mineral exploration in this belt.

5.8 Potential exploration significance

The late Eocene was a period of epithermal mineralization in the THMB and a large number of epithermal precious and base metal deposits were discovered in this belt in the vicinity of granitoid intrusions (Figure 1). These deposits are generally hosted by Eocene intermediate to acidic volcanic-volcaniclastic rocks of the Karaj Formation and are structurally controlled along the normal faults (Mehrabi et al., 2016; Kouhestani et al., 2018a; 2019a; b, 2020, 2022). The fault zones played a key role in fluid influx and ore minerals are hosted mainly by the fracture networks in the fault zone (Kouhestani et al., 2018a). Therefore, we propose that the normal faults within altered host rocks, principally at the intersection of granitoid intrusions, are suitable targets for further exploration of undiscovered epithermal deposits in the THMB. Furthermore, an understanding of mineralization systems and genetic models is crucial for the design of effective exploration strategies at the regional scale. The new data presented here indicate that Tashvir and Varmazyar are IS epithermal deposits. Consequently, the typical silica and intermediate argillic hydrothermal alteration associated with base metal mineralization may therefore provide an indication for searching for other IS epithermal deposits in the adjacent area and other parts of the THMB. Additionally, the epithermal deposits in the THMB are spatially and genetically linked to the late Eocene (40–36 Ma) granitoid intrusions (Ghasemi Siani et al., 2015; Mehrabi et al., 2016; Kouhestani et al., 2018a; 2019a; b, 2020, 2022). This relationship has provided a useful guide for exploration that could lead to the discovery of new IS mineralization adjacent to granitoid intrusions.

Given the recognition of both HS and IS epithermal mineralization in the THMB, which is usually considered the surface expression of a deeper porphyry system (Hedenquist et al., 1998, 2000; Sillitoe and Hedenquist, 2003; Seedorff et al., 2005; Valencia et al., 2008; Pudack et al., 2009; Sillitoe, 2010; Chang et al., 2011; Cooke et al., 2011; Wang L. et al., 2019), it is likely that porphyry mineralization would have the potential for prospecting at the deep sites and environs of the epithermal deposits at THMB. The Chodarchay Cu–Au deposit, characterized by the veinlet-disseminated chalcopyrite-pyrite-magnetite mineralization in the quartz monzonite overprinted by epithermal vein-type mineralization and relatively high-temperatures (up to 440°C) and high-salinity (up to 34 wt.% NaCl equivalent), was interpreted to represent a transition from porphyry to epithermal mineralization (Yasami et al., 2017; 2018; Yasami and Ghaderi, 2019). In addition, some HS (i.e., Chodarchay and north Gulojeh) and IS (i.e., Lubin-Zardeh and south Gulojeh) epithermal deposits from the THMB contain FIs features of porphyry mineralization which may be related to deeper porphyry parts of the THMB epithermal deposits (Mousavi Motlagh et al., 2019). Moreover, there are several Eocene porphyry-epithermal and related mineralization in the neighboring Ahar-Arasbaran metallogenic zone in NW Iran (Ebrahimi et al., 2011; Simmonds et al., 2017; Kouhestani et al., 2018b) and Lesser Caucasus in southern Armenia and Nakhitchevan (Moritz et al., 2016a, b; Rezeau et al., 2016) imply that the Eocene magmatic-hydrothermal metallogenic event could be favorable for porphyry Cu–Mo mineralization in NW Iran. However, pervasive advanced argillic lithocaps (including vuggy quartz and primary alunite) that are common in the upper parts of porphyry Cu–Mo systems (e.g., Cooke et al., 2005; Seedorff et al., 2005; John et al., 2010; Sillitoe, 2010), are not documented near the epithermal orebodies at THMB. Also, hypersaline (brine) FIs which are typical for porphyry-style mineralization have not been reported from the epithermal deposits in the THMB. Besides, the extensional tectonic setting of granitoid intrusions and shallow depth of magma generation from the THMB indicate that the Eocene magmatism in the THMP is less prospective for porphyry deposits (Ghasemi Siani et al., 2020). Therefore, it can be concluded that, although the possibility of

porphyry ore formation in the THMB is much rarer than in neighboring regions such as Ahar-Arasbaran and Lesser Caucasus, the lack of porphyry deposits is not obviously known or understood. More detailed work needs to be conducted in the future to constrain the genesis of the epithermal deposits and the potential existence of porphyry deposits in the THMB. Detailed geological, geochemical, and geophysical data may be able to identify drilling sites to explore deeper porphyry-type deposits in this metallogenic belt.

6 Conclusion remarks

1) Geological characteristics, FIs data, and O-S isotopic evidence show that Tashvir and Varmazyar are IS epithermal base metal deposits hosted by Eocene volcanic and volcaniclastic rocks of the Karaj Formation.
2) The crystallization ages of the granitoid intrusions at Tashvir and Varmazyar are 38.34–38.31 and 40.85 Ma, respectively, which indicates that the epithermal mineralization took place during 40.85–38.31 Ma.
3) FIs and oxygen isotope systematics suggest that the ore-forming fluids evolved from magmatic-hydrothermal fluids to dominantly meteoric water.
4) The sulfur isotopes and mineral assemblages display that ore-forming materials and sulfur are sourced mainly from a mixture of magma and surrounding sedimentary rocks.
5) Mineralization happened in response to the mixing of magmatic-hydrothermal and meteoric fluids, along with some fluid boiling.
6) The THMB is proposed to be prospective for precious and base metal epithermal mineralization. Considering the extensional tectonic setting, and lack of advanced argillic lithocaps and hypersaline FIs, the THMB possibly has less potential for economically important porphyry mineralization.

Data availability statement

The original contributions presented in the study are included in the article/supplementary material, further inquiries can be directed to the corresponding author.

Author contributions

HK and MM both contributed to field working, writing, and editing the manuscript. ZC contributed specifically to funding acquisition, review, and editing of the manuscript. KQ contributed to the discussion section, review, and editing the manuscript. SA contributed to fluid inclusion analysis, review, and editing the manuscript.

Funding

Financial support for this research provided by the office of Vice Chancellor for Research and Technology, University of Zanjan, Zanjan, Iran, and the EGRU (Economic Geology Research Centre), James Cook University, Townsville, Queensland, Australia.

Acknowledgments

We are thankful M. Ghaderi and R. Esmaeili for their help on editing U-Pb zircon dating part of the manuscript. The manuscript significantly benefited from a thorough review and constructive comments by two reviewers, and careful editorial work by H. Rezeau.

Conflict of interest

The authors declare that the research was conducted in the absence of any commercial or financial relationships that could be construed as a potential conflict of interest.

Publisher's note

All claims expressed in this article are solely those of the authors and do not necessarily represent those of their affiliated organizations, or those of the publisher, the editors and the reviewers. Any product that may be evaluated in this article, or claim that may be made by its manufacturer, is not guaranteed or endorsed by the publisher.

References

Agard, P., Omrani, J., Jolivet, L., Whitechurch, H., Vrielynck, B., Spakman, W., et al. (2011). Zagros orogeny: A subduction-dominated process. *Geol. Mag.* 148, 692–725. doi:10.1017/s001675681100046x

Aghazadeh, M., Badrzadeh, Z., and Castro, A. (2015). Petrogenesis and U-Pb SHRIMP dating of Tarom plutons. *J. Geosci.* 24 (95), 3–20. (in Persian with English abstract).

Aghazadeh, M., Castro, A., Badrzadeh, Z., and Vogt, K. (2011). Post-collisional polycyclic plutonism from the Zagros hinterland: The Shaivar Dagh plutonic complex, Alborz belt, Iran. *Geol. Mag.* 148, 980–1008. doi:10.1017/s0016756811000380

Albinson, T., Norman, D. J., Cole, D., and Chomiak, B. (2001). "Controls on formation of low-sulfidation epithermal deposits in Mexico: Constraints from fluid inclusion and stable isotope data," in *New mines and discoveries in Mexico and Central America*. Editors T. Albinson and C. E. Nelson (Econ Geol. Spec. Pub.) 8, 132.

Amini, B., Amini, M. R., Stöcklin, J., and Hirayama, K. (2001). *Geological map of Tarom, sheet no. 5763, scale 1:100, 000, 1 sheet*. Tahran, Iran: Geol. Surv. Iran.

An, F., and Zhu, Y. F. (2018). Geology and geochemistry of the early Permian Axi low-sulfidation epithermal gold deposit in north Tianshan (NW China). *Ore Geol. Rev.* 100, 12–30. doi:10.1016/j.oregeorev.2017.03.021

Arribas, A., Jr (1995). "Characteristics of high-sulfidation epithermal deposits, and their relation to magmatic fluid," in *Magmas, fluids, and ore deposits*. Editors J. F. H. Thompson (Torento, ON: Short Course), 23, 419–454.

Asiabanha, A., and Foden, J. (2012). Post-collisional transition from an extensional volcano-sedimentary basin to a continental arc in the Alborz Ranges, N-Iran. *Lithos* 148, 98–111. doi:10.1016/j.lithos.2012.05.014

Audétat, A., Pettke, T., Heinrich, C. A., and Bodnar, R. J. (2008). Special Paper: The composition of magmatic-hydrothermal fluids in barren and mineralized intrusions. *Econ. Geol.* 103, 877–908. doi:10.2113/gsecongeo.103.5.877

Azizi, H., and Jahangiri, A. (2008). Cretaceous subduction-related volcanism in the northern Sanandaj-Sirjan Zone. Iran. *J. Geodyn.* 45, 178–190. doi:10.1016/j.jog.2007.11.001

Baker, J., Peate, D., Waight, T., and Meyzen, C. (2004). Pb isotopic analysis of standards and samples using a ^{207}Pb-^{204}Pb double spike and thallium to correct for mass bias with a double-focusing MC-ICP-MS. *Chem. Geol.* 211, 275–303. doi:10.1016/j.chemgeo.2004.06.030

Baker, T. (2002). Emplacement depth and carbon dioxide-rich fluid inclusions in intrusion related gold deposit. *Econ. Geol.* 97, 1111–1117. doi:10.2113/97.5.1111

Black, L. P., and Gulson, B. L. (1978). The age of the Mud tank carbonatite, Strangways range northern Territory. *BMR J. Aust. Geol. Geoph.* 3, 227–232.

Black, L. P., Kamos, L., Allen, C. M., Aleinikoff, J. N., Davis, D. W., Korsch, R. J., et al. (2003). TEMORA 1: A new zircon standard for Phanerozoic U-Pb geochronology. *Chem. Geol.* 200, 155–170. doi:10.1016/s0009-2541(03)00165-7

Bodnar, R. J. (1993). Revised equation and table for determining the freezing point depression of H_2O-NaCl solutions. *Geochim. Cosmochim. Acta* 57, 683–684. doi:10.1016/0016-7037(93)90378-a

Bodnar, R. J., Reynolds, T. J., and Kuehn, C. A. (1985). Fluid inclusion systematics in epithermal systems. *Rev. Econ. Geol.* 2, 73–97.

Burnham, C. W. (1979). "Chapter 3: Magmas and hydrothermal fluids" in geochemistry of hydrothermal ore deposits,". Editor H. L. Barnes (John Wiley & Sons), 71–136.

Camprubi, A., and Albinson, T. (2007). Epithermal deposits in Mexico: Update of current knowledge, and an empirical reclassification. *Geol. Soc. Spec. Pup.* 422, 377–415.

Canet, C., Franco, S. I., Prol-Ledesma, R. M., González-Partida, E., and Villanueva-Estrada, R. E. (2011). A model of boiling for fluid inclusion studies: Application to the Bolaños Ag–Au–Pb–Zn epithermal deposit, Western Mexico. *J. Geochem. Explor.* 110, 118–125. doi:10.1016/j.gexplo.2011.04.005

Castro, A., Aghazadeh, M., Badrzadeh, Z., and Chichorro, M. (2013). Late Eocene-Oligocene postcollisional monzonitic intrusions from the Alborz magmatic belt, NW Iran: An example of monzonite magma generation from a metasomatised mantle source. *Lithos* 180-181, 109–127. doi:10.1016/j.lithos.2013.08.003

Chang, Z., Hedenquist, J. W., White, N. C., Cooke, D. R., Roach, M., Deyell, C. L., et al. (2011). Exploration tools for linked porphyry and epithermal deposits: Example from the Mankayan intrusion-centered Cu-Au district, Luzon, Philippines. *Econ. Geol.* 106 (8), 1365–1398. doi:10.2113/econgeo.106.8.1365

Chaussidon, M., and Lorand, J. P. (1990). Sulphur isotope composition of orogenic spinel lherzolite massifs from Ariege (North-Eastern Pyrenees, France): An ion microprobe study. *Geochim. Cosmochim. Acta* 54 (10), 2835–2846. doi:10.1016/0016-7037(90)90018-g

Cooke, D. R., Deyell, C. L., Waters, P. J., Gonzales, R. I., and Zaw, K. (2011). Evidence for magmatic-hydrothermal fluids and ore-forming processes in epithermal and porphyry deposits of the Baguio district, Philippines. *Econ. Geol.* 106 (8), 1399–1424. doi:10.2113/econgeo.106.8.1399

Cooke, D. R., Hollings, P., and Walshe, J. L. (2005). Giant porphyry deposits: Characteristics, distribution, and tectonic controls. *Econ. Geol.* 100, 801–818. doi:10.2113/gsecongeo.100.5.801

Cooke, D. R., and Simmons, S. F. (2000). Characteristics and Genesis of epithermal gold deposits. *Rev. Econ. Geol.* 13, 221–244.

Driesner, T., and Heinrich, C. A. (2007). The system H_2O-NaCl. Part I: Correlation formulae for phase relations in temperature-pressure-composition space from 0 to 1000 °C, 0 to 5000 bar, and 0 to 1 X_{NaCl}. *Geochim. Cosmochim. Acta* 71, 4880–4901. doi:10.1016/j.gca.2006.01.033

Ebrahimi, S., Alirezaei, S., and Yuanming, P. (2011). "Geological setting, alteration, and fluid inclusion characteristics of Zaglic and Safikhanloo epithermal gold prospects, NW Iran," in *Granite-related ore deposits*. Editors A. N. Sial, J. S. Bettencourt, C. P. De Campos, and V. P. Ferreira (Geological Society, London, Special Publication), 350, 33–147.

Einaudi, M. T., Hedenquist, J. W., and Inan, E. E. (2003). "Sulfidation state of fluids in active and extinct hydrothermal systems: Transitions from porphyry to epithermal environments," in *Volcanic, geothermal, and ore-forming fluids: Rulers and witnesses of processes within the Earth*. Editors S. F. Simmons and I. Graham (Littleton: Society of Economic Geologists Special Publication 10), 285–313.

Esmaeli, M., Lotfi, M., and Nezafati, N. (2015). Fluid inclusion and stable isotope study of the Khalyfehlou copper deposit, southeast Zanjan, Iran. *Arab. J. Geosci.* 8, 9625–9633. doi:10.1007/s12517-015-1907-3

Fan, H. R., Hu, F. F., Wilde, S. A., Yang, K. F., and Jin, C. W. (2011). The Qiyugou gold-bearing breccia pipes, Xiong'ershan region, central China: Fluid-inclusion and stable-isotope evidence for an origin from magmatic fluids. *Int. Geol. Rev.* 53, 25–45. doi:10.1080/00206810902875370

Faridi, M., and Anvari, A. (2000). *Geological map of hashtjin, sheet no. 5664, scale 1:100,000, 1 sheet*. Tehran, Iran: Geol. Surv. Iran.

Field, C. W., and Fifarek, R. H. (1985). Light stable isotope systematics in epithermal systems. *Rev. Econ. Geol.* 2, 99–128.

Figueroa, A. J. T., Gabo-Ratio, J. A. S., Manalo, P. C., Takahashi, R., Sato, H., and Ramos, A. B. (2022). Breccia and vein mineralization of the Balatoc Diatreme, Acupan gold deposit, Baguio Mineral District: An example of a diatreme-hosted epithermal deposit in the Philippines. *Ore Geol. Rev.* 144, 104826. doi:10.1016/j.oregeorev.2022.104826

Gemmell, J. B. (2004). "Low- and intermediate-sulfidation epithermal deposits," in *24 carat gold workshop*. Editors D. R. Cooke, C. L. Deyell, and J. Pongratz (Hobart, TAS: Centre for Ore Depeposit Resource Special Publication), 5, 57–63.

Ghasemi Siani, M., Lentz, D. R., and Nazarian, M. (2020). Geochemistry of igneous rocks associated with mineral deposits in the Tarom-Hashtjin metallogenic province, NW Iran: An analysis of the controls on epithermal and related porphyry-style mineralization on epithermal and related porphyry-style mineralization103753. *Ore Geol. Rev.* 126, 103753. doi:10.1016/j.oregeorev.2020.103753

Ghasemi Siani, M., Mehrabi, B., Azizi, H., Wilkinson, C. M., and Ganerod, M. (2015). Geochemistry and geochronology of the volcano-plutonic rocks associated with the Glojeh epithermal gold mineralization, NW Iran. *Open Geosci.* 7, 207–222. doi:10.1515/geo-2015-0024

Ghasemi Siani, M., Mehrabi, B., Nazarian, M., Lotfi, M., and Corfu, F. (2022). Geology and Genesis of the Chomalu polymetallic deposit, NW Iran. *Ore Geol. Rev.* 143, 104763. doi:10.1016/j.oregeorev.2022.104763

Ghorbani, A. (2020). *Geology, geochemistry and Genesis of Varmazyar Pb-Zn (Ag) mineralization*. Zanjan, Iran: University of Zanjan. north of Zanjan. [dissertation/master's thesis]. (in Persian with English abstract).

Ghorbani, A., Kouhestani, H., and Mokhtari, M. A. A. (2022). Genesis of the Varmazyar Pb-Zn (Ag) occurrence, Tarom-Hashtjin metallogenic belt: Insights from ore geology, geochemistry and fluid inclusion studies. *J. Econ. Geol.* 14 (1), 1–38. (in Persian with extended English abstract).

Goldstein, R. H. (2003). "Petrographic analysis of fluid inclusions," in *Fluid inclusions: Analysis and interpretation*. Editors I. Samson, A. Anderson, and D. Marshall (Torento, ON: Mineralogical Association of Canada, Short Course), 32, 9–53.

Goldstein, R. H., and Reynolds, T. J. (1994). *Systematics of fluid inclusions in diagenetic minerals*. Tulsa, Oklahoma: Society for Sedimentary Geology SEPM.

Guimarães, S. B., Klein, E. L., Harris, C., and Costa, I. S. L. (2021). Metallogenesis of the Orosirian epithermal Coringa gold-silver (Cu-Pb-Zn) deposit, southeastern Tapajos ´ mineral Province, Amazonian craton, Brazil. *Ore Geol. Rev.* 128, 103908. doi:10.1016/j.oregeorev.2020.103908

He, X., Yu, Q., Liu, S., Yang, M., and Zhang, D. (2021). Origin of the Erdaohe Ag-Pb-Zn deposit, central Great Xing'an Range, northeast China: Constraints from fluid inclusions, zircon U-Pb geochronology, and stable isotopes. *Ore Geol. Rev.* 137, 104309. doi:10.1016/j.oregeorev.2021.104309

Heald, P., Foley, N. K., and Hayba, D. O. (1987). Comparative anatomy of volcanic-hosted epithermal deposits: Acid-sulfate and adularia-sericite types. *Econ. Geol.* 82 (1), 1–26. doi:10.2113/gsecongeo.82.1.1

Hedenquist, J. W., Arribas, A., and Reynolds, T. J. (1998). Evolution of an intrusion-centered hydrothermal system; Far Southeast-Lepanto porphyry and epithermal Cu-Au deposits, Philippines. *Econ. Geol.* 93 (4), 373–404. doi:10.2113/gsecongeo.93.4.373

Hedenquist, J. W., Arribas, A. R., and Gonzalez-Urien, E. (2000). Exploration for epithermal gold deposits. *Rev. Econ. Geol.* 13, 245–277.

Hedenquist, J. W., and Henley, R. W. (1985). The importance of CO_2 on freezing point measurements of fluid inclusions: Evidence from active geothermal systems and implications for epithermal ore deposition. *Econ. Geol.* 80, 1379–1406. doi:10.2113/gsecongeo.80.5.1379

Hedenquist, J. W., and Lowenstern, J. B. (1994). The role of magmas in the formation of hydrothermal ore deposits. *Nature* 370, 519–527. doi:10.1038/370519a0

Henley, R. W., and Berger, B. R. (2011). Magmatic-vapor expansion and the formation of high-sulfidation gold deposits: Chemical controls on alteration and mineralization. *Ore Geol. Rev.* 39, 63–74. doi:10.1016/j.oregeorev.2010.11.003

Henley, R. W. (1985). The geothermal framework for epithermal deposits. *Rev. Econ. Geol.* 2, 1–21.

Henning, D., Lehmann, B., Burgess, R., and Mohammad, A. N. T. (2008). Geology, geochemistry and $^{40}Ar/^{39}Ar$ ages of the Cerro Millo epithermal high-sulfidation gold prospect, southern Peru. *Ore Geol. Rev.* 34 (3), 304–316. doi:10.1016/j.oregeorev.2008.02.001

Hoefs, J. (2018). *Stable isotope geochemistry*. Berlin Heidelberg: Springer-Verlag.

Hou, Z. Q., and Wang, E. Q. (2008). Metallogenesis of the Indo-Asian collisional orogen: New advances. *Acta Geosci. Sin.* 29 (3), 275–292.

Hou, Z., and Zhang, H. (2015). Geodynamics and metallogeny of the eastern Tethyan metallogenic domain. *Ore Geol. Rev.* 70, 346–384. doi:10.1016/j.oregeorev.2014.10.026

Jackson, S. E., Pearson, N. J., Griffin, W. L., and Belousova, E. A. (2004). The application of laser ablation-inductively coupled plasma-mass spectrometry to *in situ* U-Pb zircon geochronology. *Chem. Geol.* 211, 47–69. doi:10.1016/j.chemgeo.2004.06.017

Jébrak, M. (1997). Hydrothermal breccias in vein-type ore deposits: A review of mechanisms, morphology and size distribution. *Ore Geol. Rev.* 12, 111–134. doi:10.1016/s0169-1368(97)00009-7

Jobson, D. H., Boulter, C. A., and Foster, R. P. (1994). Structural controls and Genesis of epithermal gold-bearing breccias at the Lebong Tandai mine, Western Sumatra. Indonesia. *J. Geochem. Explor.* 50, 409–428. doi:10.1016/0375-6742(94)90034-5

John, D. A., Ayuso, R. A., Barton, M. D., Blakely, R. J., Bodnar, R. J., Dilles, J. H., et al. (2010). *Porphyry copper deposit model. Chap. B of Mineral deposit models for resource assessment, U.S.* Geological Survey Scientific Investigations Report 2010–5070–B, 169.

John, D. A., Hofstra, A. H., Fleck, R. E., Brummer, J. E., and Saderholm, E. C. (2003). Geologic setting and genesis of the Mule Canyon low-sulfidation epithermal gold-silver deposit, north-central Nevada. *Econ. Geol.* 98 (2), 425–463. doi:10.2113/gsecongeo.98.2.425

John, D. A. (2001). Miocene and early Pliocene epithermal gold-silver deposits in the northern great basin, western United States: Characteristics, distribution, and relationship to magmatism. *Econ. Geol.* 96, 1827–1853. doi:10.2113/gsecongeo.96.8.1827

Johnson, P. R. (2021). "The Arabian-nubian Shield, an introduction: Historic Overview, concepts, interpretations, and future Issues," in *The geology of the arabian-nubian shield, regional geology reviews*. Editors Z. Hamimi, A. R. Fowler, J. P. Liégeois, A. Collins, M. G. Abdelsalam, and M. Abd El-Wahed (Cham: Springer), 1–38.

Kargaran Bafghi, F., and Neubauer, F. (2015). Lithospheric thinning associated with formation of a metamorphic core complex and subsequent formation of the Iranian plateau. *GSA Today* 25, 4–8. doi:10.1130/gsatg229a.1

Karimpouli, S. (2017). *Exploration report of Pb-Zn in Varmazyar area*. Iran: Industry, Mine and Trade Organization of Zanjan. Zanjan. (in Persian).

Kirk, J. D., Ruiz, J., Kesler, S. E., Simon, A., and Muntean, J. L. (2014). Re-Os age of the Pueblo Viejo epithermal deposit, Dominican Republic. *Econ. Geol.* 109 (2), 503–512. doi:10.2113/econgeo.109.2.503

Koch, P. L., Zachos, J. C., and Dettman, D. L. (1995). Stable isotope stratigraphy and paleoclimatology of the Paleogene Bighorn Basin, (Wyoming, U.S.A.). *Palaeogeogr. Palaeoclimatol. Palaeoecol.* 115, 61–89. doi:10.1016/0031-0182(94)00107-j

Kosler, J. (2001). "Laser-ablation ICP–MS study of metamorphic minerals and processes," in *Laser-ablation-ICP-MS in the Earth sciences*. Editor P. J. Sylvester (Vancouver, BC: Principles and applications, Mineralogical Association of Canada), 185–202. Short Course Handbook 29.

Kouhestani, H., Azimzadeh, A. M., Mokhtari, M. A. A., and Ebrahimi, M. (2017). Mineralization and fluid evolution of epithermal base metal veins from the Aqkand deposit, NW Iran. *njma*. 194 (2), 139–155. doi:10.1127/njma/2017/0036

Kouhestani, H. (2016). *Exploration report of Pb-Zn-Cu in Tashvir area*. Iran: Industry, Mine and Trade Organization of Zanjan. Zanjan. (in Persian).

Kouhestani, H., Ghaderi, M., Chang, Z., and Zaw, K. (2015). Constraints on the ore fluids in the Chah Zard breccia-hosted epithermal Au-Ag deposit, Iran: Fluid inclusions and stable isotope studies. *Ore Geol. Rev.* 65, 512–521. doi:10.1016/j.oregeorev.2013.06.003

Kouhestani, H., Mokhtari, M. A. A., and Chang, Z. (2022). Fluid inclusion and stable isotope constraints on the Genesis of epithermal base-metal veins in the Armaqan Khaneh mining district, Tarom-Hashtjin metallogenic belt, NW Iran. *Aust. J. Earth Sci.* 69 (6), 844–860. doi:10.1080/08120099.2022.2033320

Kouhestani, H., Mokhtari, M. A. A., Chang, Z., and Johnson, A. C. (2018a). Intermediate sulfidation type base metal mineralization at Aliabad-Khanchy, Tarom-Hashtjin metallogenic belt, NW Iran. *Ore Geol. Rev.* 93, 1–18. doi:10.1016/j.oregeorev.2017.12.012

Kouhestani, H., Mokhtari, M. A. A., Chang, Z., Stein, H. J., and Johnson, A. C. (2018b). Timing and Genesis of ore formation in the Qarachilar Cu-Mo-Au deposit, Ahar-Arasbaran metallogenic zone, NW Iran: evidence from geology, fluid inclusions, O-S isotopes and Re-Os geochronology. *Ore Geol. Rev.* 102, 757–775. doi:10.1016/j.oregeorev.2018.10.007

Kouhestani, H., Mokhtari, M. A. A., Qin, K. Z., and Zhang, X. N. (2020). Genesis of the Abbasabad epithermal base metal deposit, NW Iran: Evidences from ore geology, fluid inclusion and O-S isotopes. *Ore Geol. Rev.* 126, 103752. doi:10.1016/j.oregeorev.2020.103752

Kouhestani, H., Mokhtari, M. A. A., Qin, K. Z., and Zhao, J. X. (2019a). Fluid inclusion and stable isotope constraints on ore Genesis of the Zajkan epithermal base metal deposit, Tarom-Hashtjin metallogenic belt. NW Iran. *Ore Geol. Rev.* 109, 564–584. doi:10.1016/j.oregeorev.2019.05.014

Kouhestani, H., Mokhtari, M. A. A., Qin, K. Z., and Zhao, J. X. (2019b). Origin and evolution of hydrothermal fluids in the Marshoun epithermal Pb-Zn-Cu (Ag) deposit, Tarom-Hashtjin metallogenic belt. NW Iran. *Ore Geol. Rev.* 113, 103087. doi:10.1016/j.oregeorev.2019.103087

Kouhestani, H., and Mokhtari, M. A. A. (2019). Tashvir ore occurrence, NE Zanjan: Intermediate-sulfidation style of epithermal base metal (Ag) mineralization in the Tarom–Hashtjin zone. *J. Geosci.* 28 (110), 97–108. (in Persian with English abstract).

Kouhestani, H. (2018). *Temporal–spatial relationships between epithermal mineralization and Eocene magmatism at the Tarom-Hashtjin region, Tethyan metallogenic belt, northwestern Iran*. Beijing, China: Institute of Geology and Geophysics, Chinese Academy of Sciences.

Li, Y. B., and Liu, J. M. (2006). Calculation of sulfur isotope fractionation in sulfides. *Geochim. Cosmochim. Acta* 70, 1789–1795.

Lei, X. F., Duan, D. F., Jiang, S. Y., and Xiong, S. F. (2018). Ore-forming fluids and isotopic (H-O-C-S-Pb) characteristics of the Fujiashan-Longjiaoshan skarn W-Cu-(Mo) deposit in the Edong District of Hubei Province, China Hubei Province, China. *Ore Geol. Rev.* 102, 386–405. doi:10.1016/j.oregeorev.2018.09.019

Li, H., Tang, J., Hu, G., Ding, S., Li, Z., Xie, F., et al. (2019). Fluid inclusions, isotopic characteristics and geochronology of the Sinongduo epithermal Ag-Pb-Zn deposit, Tibet, China. *Ore Geol. Rev.* 107, 692–706. doi:10.1016/j.oregeorev.2019.02.033

Li, S. N., Ni, P., Bao, T., Li, C. Z., Xiang, H. L., Wang, G. G., et al. (2018). Geology, fluid inclusion, and stable isotope systematics of the Dongyang epithermal gold deposit, Fujian Province, southeast China: Implications for ore Genesis and mineral exploration. *J. Geochem. Explor.* 195, 16–30. doi:10.1016/j.gexplo.2018.02.009

Li, Y. S., Lv, Z. C., Yan, G. S., Zhen, S. M., and Du, Z. Z. (2012). Isotopic characteristics of S, Pb, H and O of Jiama copper-polymetallic ore deposit, Tibet and their significance. *Earth Sci. Front.* 19 (4), 072–081.

Liu, C. F., Zhao, S. H., and Liu, W. (2021). The relationship between gold mineralization, high K calc-alkaline to alkaline volcanic rocks, and A-type granite: Formation of the Daxiyingzi gold deposit in northern North China Craton. *Ore Geol. Rev.* 138, 104383. doi:10.1016/j.oregeorev.2021.104383

Liu, T., Xiong, S. F., Jiang, S. Y., Li, H. L., Chen, Q. Z., and Jiang, H. (2017). Genesis of the Zhijiadi Ag-Pb-Zn deposit, central North China Craton: constraints from fluid inclusions and stable isotope data. *Geofluids* 2017, 1–23. doi:10.1155/2017/4153618

Ludwig, K. R. (1998). *Isoplot: A plotting and regression program for radiogenic isotope data*. version 3.00.

Matsuhisa, Y., and Aoki, M. (1994). Temperature and oxygen isotope variations during formation of the Hishikari epithermal gold-silver veins, southern Kyushu, Japan. *Econ. Geol.* 89, 1608–1613. doi:10.2113/gsecongeo.89.7.1608

Matsuhisa, Y., Goldsmith, J. R., and Clayton, R. N. (1979). Oxygen isotopic fractionation in the system quartz-albite-anothite-water. *Geochim. Cosmochim. Acta* 43, 1131–1140.

Meffre, S., Large, R. R., Scott, R., Woodhead, J., Chang, Z., Gilbert, S. E., et al. (2008). Age and pyrite Pb-isotopic composition of the giant Sukhoi Log sediment-hosted gold deposit Russia. *Geochim. Cosmochim. Acta* 72, 2377–2391. doi:10.1016/j.gca.2008.03.005

Mehrabi, B., Ghasemi Siani, M., Goldfarb, R., Azizi, H., Ganerod, M., and Marsh, E. E. (2016). Mineral assemblages, fluid evolution and Genesis of polymetallic epithermal veins, Gulojeh district, NW Iran. *Ore Geol. Rev.* 78, 41–57.

Mikaeili, K., Hosseinzadeh, M. R., Moayyed, M., and Maghfouri, S. (2018). The Shah-AliBeiglou Zn-Pb-Cu (Ag) deposit, Iran: An example of intermediate-sulfidation epithermal type mineralization. *Miner. (Basel).* 8 (4), 148. doi:10.3390/min8040148

Mokhtari, M. A. A., Kouhestani, H., and Gholizadeh, K. (2019). Mineral chemistry and formation conditions of calc-silicate minerals of Qozlou Fe skarn deposit, Zanjan Province, NW Iran. *Arab. J. Geosci.* 12 (21), 658–723. doi:10.1007/s12517-019-4814-1

Mokhtari, M. A. A., Kouhestani, H., Pang, K. N., Hsu, S. C., Chung, S. L., and Lee, H. Y. (2022b). Early Eocene high-Sr/Y magmas from the Urumieh-Dokhtar paleo-arc, Iran: Implications for the origin of high-flux events in magmatic arcs. *Lithos* 416–417, 106656. doi:10.1016/j.lithos.2022.106656

Mokhtari, M. A. A., Kouhestani, H., and Qin, K. Z. (2022a). Zircon U-Pb age, whole-rock geochemistry and Nd-Sr-Pb isotope constraints on petrogenesis of the Eocene Zajkan gabbro-monzogranite intrusion, Tarom-Hashtjin magmatic belt, NW Iran. *Aust. J. Earth Sci.* 69 (7), 1030–1047. doi:10.1080/08120099.2022.2068648

Moncada, D., Baker, D., and Bodnar, R. J. (2017). Mineralogical, petrographic and fluid inclusion evidence for the link between boiling and epithermal Ag-Au mineralization in the La Luz area, Guanajuato Mining District, México. *Ore Geol. Rev.* 89, 143–170. doi:10.1016/j.oregeorev.2017.05.024

Moncada, D., Mutchler, S., Nieto, A., Reynolds, T. J., Rimstidt, J. D., and Bodnar, R. J. (2012). Mineral textures and fluid inclusion petrography of the epithermal Ag-Au deposits at Guanajuato, Mexico: Application to exploration. *J. Geochem. Explor.* 114, 20–35. doi:10.1016/j.gexplo.2011.12.001

Moritz, R., Melkonyan, R., Selby, D., Popkhadze, N., Gugushvili, V., Tayan, R., et al. (2016a). Metallogeny of the Lesser Caucasus: from arc construction to postcollision evolution. *Econ. Geol. Spec. Publ.* 19, 157–192.

Moritz, R., Rezeau, H., Ovtcharova, M., Tayan, R., Melkonyan, R., Hovakimyan, S., et al. (2016b). Long-lived, stationary magmatism and pulsed porphyry systems during Tethyan subduction to post-collision evolution in the southernmost Lesser Caucasus, Armenia and Nakhitchevan. *Gondwana Res.* 37, 465–503. doi:10.1016/j.gr.2015.10.009

Mousavi Motlagh, S. H., and Ghaderi, M. (2019). The Chargar Au-Cu deposit: an example of low-sulfidation epithermal mineralization from the Tarom subzone, NW Iran. *njma.* 196 (1), 43–66. doi:10.1127/njma/2019/0158

Mousavi Motlagh, S. H., Ghaderi, M., Yasami, N., and Alfonso, P. (2019). Stable isotope geochemistry of Chargar epithermal deposit: Constraints on epithermal systems in the Tarom metallogenic belt. NW Iran. *J. Geochem. Explor.* 205, 106331. doi:10.1016/j.gexplo.2019.06.013

Mousavi Motlagh, S. H., Ghaderi, M., and Yasami, N. (2021). Porphyry-type mineralization associated with epithermal deposits in the Tarom metallogenic belt of NW Iran: Constraints from fluid inclusions. *J. Geochem. Explor.* 223, 106724. doi:10.1016/j.gexplo.2021.106724

Nabatian, G., Ghaderi, M., Neubauer, F., Honarmandc, M., Xiaoming, L., Dong, Y., et al. (2014). Petrogenesis of Tarom high-potassic granitoids in the Alborz-Azarbaijan belt, Iran: Geochemical, U-Pb zircon and Sr-Nd-Pb isotopic constraints. *Lithos* 184-187, 324–345. doi:10.1016/j.lithos.2013.11.002

Nabatian, G., Jiang, S. Y., Honarmand, M., and Neubauer, F. (2016). Zircon U-Pb ages, geochemical and Sr-Nd-Pb-Hf isotopic constraints on petrogenesis of the Tarom-Olya pluton, Alborz magmatic belt, NW Iran. *Lithos* 244, 43–58. doi:10.1016/j.lithos.2015.11.020

Niu, P. P., and Jiang, S. Y. (2022). Fluid inclusion and stable isotope (C-H-O-S) constraints on the Genesis of the Heilongtan-Xiejiagou Au deposit, northern Hubei, China. *Ore Geol. Rev.* 144, 104841. doi:10.1016/j.oregeorev.2022.104841

Ohmoto, H., and Goldhaber, M. B. (1997). "Sulfur and carbon isotopes," in *Geochemistry of hydrothermal ore deposits*. Editor H. L. Barnes (John Wiley & Sons), 17–611.

Ohmoto, H., and Rye, R. O. (1979). "Isotope of sulfur and carbon," in *Geochemistry of hydrothermal ore deposits*. Editor H. L. Barnes (John Wiley & Sons), 509–567.

Ohmoto, H. (1986). Stable isotope geochemistry of ore deposits. *Rev. Mineral. Geochem.* 16, 491–559.

Ohmoto, H. (1972). Systematics of sulfur and carbon isotopes in hydrothermal ore deposits. *Econ. Geol.* 67, 551–578. doi:10.2113/gsecongeo.67.5.551

Oyman, T. (2019). "Epithermal Deposits of Turkey," in *Mineral resources of Turkey*. Editors F. T. Pirajno, C. Ünlü, M. Dönmez, and Şahin (Gewerbestrasse, Switzerland: Modern Approaches in Solid Earth Sciences), 16, 159–223.

Pass, H. E., Cooke, D. R., Davidson, G., Maas, R., Dipple, G., Rees, C., et al. (2014). Isotope geochemistry of the northeast zone, Mount Polley alkalic Cu-Au-Ag porphyry deposit, British Columbia: A case for carbonate assimilation. *Econ. Geol.* 109, 859–890. doi:10.2113/econgeo.109.4.859

Pearson, M. F., Clark, K. F., Porter, E. W., and Gonzalez, S. O. (1988). Mineralogy, fluid characteristics, and silver distribution at Real de Angeles, Zacatecas. *Econ. Geol.* 83, 1737–1759. doi:10.2113/gsecongeo.83.8.1737

Peng, Y. E., Gu, X. X., Chi, G. X., Zhang, Y. M., Zhao, K. P., Zheng, L., et al. (2021). Fluid inclusions, isotopes and mineralogy of the Kuruer epithermal Cu-Au deposit, Chinese Western Tianshan: Implications for ore Genesis and exploration. *Ore Geol. Rev.* 139A, 104385. doi:10.1016/j.oregeorev.2021.104385

Pudack, C., Halter, W. E., Heinrich, C. A., and Pettke, T. (2009). Evolution of magmatic vapor to gold-rich epithermal liquid: the porphyry to epithermal transition at Nevados de Famatina, northwest Argentina. *Econ. Geol.* 104 (4), 449–477. doi:10.2113/gsecongeo.104.4.449

Qin, K. Z., and Ishihara, S. (1998). On the Possibility of Porphyry Copper Mineralization in Japan. *Int. Geol. Rev.* 40, 539–551. doi:10.1080/00206819809465223

Qin, K. Z., Sun, S., Li, J. L., Fang, T. H., Wang, S. L., and Liu, W. (2002). Paleozoic epithermal Au and porphyry Cu deposits in North Xinjiang, China: Epochs, features, tectonic linkage and exploration significance. *Resour. Geol.* 52, 291–300. doi:10.1111/j.1751-3928.2002.tb00140.x

Rabiei, M., Chi, G., Normand, C., Davis, W. J., Fayek, M., and Blamey, N. J. F. (2017). Hydrothermal rare Earth element (Xenotime) mineralization at Maw Zone, Athabasca Basin, Canada, and its relationship to unconformity-related uranium deposits. *Econ. Geol.* 112, 1483–1507. doi:10.5382/econgeo.2017.4518

Rezeau, H., Moritz, R., Wotzlaw, J. F., Tayan, R., Melkonyan, R., Ulianov, A., et al. (2016). Temporal and genetic link between incremental pluton assembly and pulsed porphyry Cu–Mo formation in accretionary orogens. *Geology* 44, 627–630. doi:10.1130/g38088.1

Richards, J. P. (2015). Tectonic, magmatic, and metallogenic evolution of the Tethyan orogen: From subduction to collision. *Ore Geol. Rev.* 70, 323–345. doi:10.1016/j.oregeorev.2014.11.009

Robinson, B. W., and Kusakabe, M. (1975). Quantitative preparation of sulfur dioxide, for $^{34}S/^{32}S$ analyses, from sulfides by combustion with cuprous oxide. *Anal. Chem.* 47, 1179–1181. doi:10.1021/ac60357a026

Roedder, E., and Bodnar, R. J. (1980). Geologic pressure determinations from fluid inclusion studies. *Annu. Rev. Earth Planet. Sci.* 8, 263–301. doi:10.1146/annurev.ea.08.050180.001403

Roedder, E. (1984). *Fluid inclusions rev. Mineral.*, 12. Washington, D.C.: Mineral. Soc. Am.

Rollinson, H. R. (1993). *Using geochemical data: Evaluation, presentation, interpretation*. United Kingdom: Longman.

Rusk, B. G., Reed, M. H., and Dilles, J. H. (2008). Fluid inclusion evidence for magmatic-hydrothermal fluid evolution in the porphyry copper-molybdenum deposit at Butte, Montana. *Econ. Geol.* 103 (2), 307–334. doi:10.2113/gsecongeo.103.2.307

Seal, I. R., and Rye, R. O. (1993). Stable isotope study of fluid inclusions in fluorite from Idaho: Implications for continental climates during the Eocene. *Geol.* 21, 219–222. doi:10.1130/0091-7613(1993)021<0219:sisofi>2.3.co;2

Seal, I. R. (2006). Sulfur isotope geochemistry of sulfide minerals. *Rev. Mineral. Geochem.* 61, 633–677. doi:10.2138/rmg.2006.61.12

Searle, M. P., Robb, L. J., and Gardiner, N. J. (2016). Tectonic processes and metallogeny along the Tethyan mountain ranges of the Middle East and south Asia (Oman, Himalaya, Karakoram, Tibet, Myanmar, Thailand, Malaysia). *Spec. Publ.* 19, 301–327.

Seedorff, E., Dilles, J. H., Proffett, J. M., Einaudi, M. T., Zurcher, L., Stavast, W. J. A., et al. (2005). "Porphyry deposits: characteristics and origin of hypogene features," in *Economic geology one hundredth anniversary volume*. Editors J. W. Hedenquist, J. F. H. Thompson, R. J. Goldfarb, and J. P. Richards (Littleton: Society of Economic Geologists), 251–298.

Shafaii Moghadam, H., Griffin, W. L., Kirchenbaur, M., Garbe-Schonberg, D., Zakie Khedr, M., Kimura, J. I., et al. (2018). Roll-back, extension and mantle upwelling triggered Eocene potassic magmatism in NW Iran. *J. Petrology* 59, 1417–1465. doi:10.1093/petrology/egy067

Shahbazi, S., Ghaderi, M., and Alfonso, P. (2019). Mineralogy, alteration, and sulfur isotope geochemistry of the Zehabad intermediate-sulfidation epithermal deposit. NW Iran. *Tur. J. Earth Sci.* 28, 882–901.

Sharp, Z. D. (1990). A laser-based microanalytical method for the *in-situ* determination of oxygen isotope ratios of silicates and oxides. *Geochim. Cosmochim. Acta* 54, 1353–1357. doi:10.1016/0016-7037(90)90160-m

Sheppard, S. M. F. (1986). Characterization and isotopic variations in natural waters. *Rev. Min. Geochem.* 16, 165–183.

Shi, G., Xue, J., Zhu, X., Pang, Z., Wang, X., Yang, F., et al. (2022). Ore Genesis of the Changkeng–Fuwan Au-Ag deposit in central Guangdong, south China: Evidence from fluid inclusions and C-H-O-S-Pb-He-Ar isotopes. *Minerals* 12, 799. doi:10.3390/min12070799

Sillitoe, R. H., and Hedenquist, J. W. (2003). Linkages between volcano-tectonic settings, ore fluid compositions, and epithermal precious metal deposits. *Econ. Geol. Spec. Pub.* 10, 315–343.

Sillitoe, R. H. (2010). Porphyry copper systems. *Econ. Geol.* 105, 3–41. doi:10.2113/gsecongeo.105.1.3

Simmonds, V., Moazzen, M., and Mathur, R. (2017). Constraining the timing of porphyry mineralization in northwest Iran in relation to Lesser Caucasus and Central Iran; Re-Os age data for Sungun porphyry Cu–Mo deposit. *Int. Geol. Rev.* 59 (12), 1561–1574. doi:10.1080/00206814.2017.1285258

Simmons, S. F., and Brown, K. L. (2006). Gold in magmatic-hydrothermal solutions and the rapid formation of a Giant ore deposit. *Science* 314, 288–291. doi:10.1126/science.1132866

Simmons, S. F., White, N. C., and John, D. A. (2005). "Geological characteristics of epithermal precious and base metal deposits," in *Economic geology one hundredth anniversary volume*. Editors J. W. Hedenquist, J. F. H. Thompson, R. J. Goldfarb, and J. P. Richards (Littleton: Society of Economic Geologists), 485–522.

Soberano, O. B., Gabo-Ratio, J. A. S., Queano, K. L., Dimalanta, C. B., Yumul, G. P., Jr., Andal, E. S., et al. (2021). Mineral chemistry, fluid inclusion and stable isotope studies of the Suyoc epithermal veins: Insights to Au-Cu mineralization in southern Mankayan mineral district, Philippines. *Ore Geol. Rev.* 131, 104035. doi:10.1016/j.oregeorev.2021.104035

Stefansson, A., and Seward, T. M. (2003). Experimental determination of the stability and stoichiometry of sulphide complexes of silver (I) in hydrothermal solutions to 400 °C. *Geochim. Cosmochim. Acta* 67, 1395–1413. doi:10.1016/s0016-7037(02)01093-1

Sun, G., Zeng, Q., Zhou, J. X., Zhou, L. F., and Chen, P. (2021). Genesis of the Xinling vein-type Ag-Pb-Zn deposit, Liaodong Peninsula, China: Evidence from texture, composition and *in situ* S-Pb isotopes. *Ore Geol. Rev.* 133, 104120. doi:10.1016/j.oregeorev.2021.104120

Taylor, H. P. (1974). The application of oxygen and hydrogen isotope studies to problems of hydrothermal alteration and ore deposition. *Econ. Geol.* 69, 843–883. doi:10.2113/gsecongeo.69.6.843

Thiersch, P. C., Williams-Jones, A. E., and Clark, J. R. (1997). Epithermal mineralization and ore controls of the Shasta Au–Ag deposit, Toodoggone District, British Columbia, Canada. *Min. Depos.* 32, 44–57. doi:10.1007/s001260050071

Tindell, T., Watanabe, K., Imai, A., Takahashi, R., Boyce, A. J., Yonezu, K., et al. (2018). The Kago low-sulfidation gold and silver deposit: A peripheral mineralisation to the Nansatsu high-sulfidation system, southern Kyushu, Japan. *Ore Geol. Rev.* 102, 951–966. doi:10.1016/j.oregeorev.2017.10.027

Ulrich, T., Gunther, D., and Heinrich, C. A. (2001). The evolution of a porphyry Cu-Au deposit based on LA-ICP-MS analysis of fluid inclusions: Bajo de la Alumbrera. Argentina. *Econ. Geol.* 96, 1743–1774. doi:10.2113/gsecongeo.96.8.1743

Valencia, V. A., Eastoe, C., Ruiz, J., Ochoa-Landin, L., Gehrels, G., Gonzalez-Leon, C., et al. (2008). Hydrothermal evolution of the porphyry copper deposit at La Caridad, Sonora, Mexico, and the relationship with a neighboring high-sulfidation epithermal deposit. *Econ. Geol.* 103, 473–491. doi:10.2113/gsecongeo.103.3.473

Verdel, C., Wernicke, B. P., Hassanzadeh, J., and Guest, B. (2011). A Paleogene extensional arc flare-up in Iran. *Tectonics* 30 (3). doi:10.1029/2010tc002809

Wang, L., Qin, K. Z., Song, G. Y., and Li, G. M. (2019a). A review of intermediate sulfidation epithermal deposits and subclassification. *Ore Geol. Rev.* 107, 434–456. doi:10.1016/j.oregeorev.2019.02.023

Wang, X., Ren, Y., Zhao, D., and Ren, X. (2019b). Ore-forming fluids and ore Genesis of the large Bayanbaolege Ag polymetallic deposit, Southern Great Xing'an Range, NE China. *Ore Geol. Rev.* 111, 102987. doi:10.1016/j.oregeorev.2019.102987

White, N. C., and Hedenquist, J. W. (1990). Epithermal environments and styles of mineralization: Variations and their causes, and guidelines for exploration. *J. Geochem. Explor.* 36, 445–474. doi:10.1016/0375-6742(90)90063-g

White, N. C., and Hedenquist, J. W. (1995). Epithermal gold deposits: Styles, characteristics and exploration. *Seg. Discov.* 27, 1–13. doi:10.5382/segnews.1995-23.fea

White, N. C., Leake, M. J., McCaughey, S. N., and Parris, B. W. (1995). Epithermal gold deposits of the southwest Pacific. *J. Geochem. Explor.* 54, 87–136. doi:10.1016/0375-6742(95)00027-6

Whitney, D. L., and Evans, B. W. (2010). Abbreviations for names of rock-forming minerals. *Am. Mineral.* 95, 185–187. doi:10.2138/am.2010.3371

Wiendenbeck, M., Alle, P., Corfu, F., Griffin, W. L., Meier, M., Oberli, F., et al. (1995). 3 Natural zircon standards for U-Th-Pb-Lu-Hf trace-element and REE analyses. *Geostand. Newsl.* 19, 1–23.

Wilkinson, J. J. (2001). Fluid inclusions in hydrothermal ore deposits. *Lithos* 55, 229–272. doi:10.1016/s0024-4937(00)00047-5

Williams-Jones, A. E., and Migdisov, A. A. (2014). Experimental constraints on the transport and deposition of metals in ore-forming hydrothermal systems. *Econ. Geol.* 18, 77–96.

Xie, Y., Li, L., Wang, B., Li, G., Liud, H., Li, Y., et al. (2017). Genesis of the Zhaxikang epithermal Pb-Zn-Sb deposit in southern Tibet, China: evidence for a magmatic link. *Ore Geol. Rev.* 80, 891–909. doi:10.1016/j.oregeorev.2016.08.007

Xu, Z. K., Sun, J. G., Liu, Y., Han, J. L., Xu, Z. T., and Liang, X. L. (2021). Geology, fluid inclusion and H-O-S-Pb isotope study of the Ganhegou epithermal gold deposit in Yanbian, NE China: Implications for ore Genesis and mineralization process. *Ore Geol. Rev.* 135, 104199. doi:10.1016/j.oregeorev.2021.104199

Yang, J. J., Yang, X., Yang, C. D., Li, Q., and Yang, F. (2022). Genesis of the Talate Pb-Zn (Fe) deposit in the Altay, Xinjiang, NW China: Evidence from fluid inclusions and stable isotopes. *Ore Geol. Rev.* 144, 104864. doi:10.1016/j.oregeorev.2022.104864

Yardley, B. W. D. (2005). Metal concentrations in crustal fluids and their relationship to ore formation. *Econ. Geol.* 100, 613632.

Yasami, N., Ghaderi, M., and Alfonso, P. (2018). Sulfur isotope geochemistry of the Chodarchay Cu-Au deposit, Tarom, NW Iran. *njma.* 195 (2), 101–113. doi:10.1127/njma/2018/0097

Yasami, N., and Ghaderi, M. (2019). Distribution of alteration, mineralization and fluid inclusion features in porphyry-high sulfidation epithermal systems: The Chodarchay example, NW Iran. *Ore Geol. Rev.* 104, 227–245. doi:10.1016/j.oregeorev.2018.11.006

Yasami, N., Ghaderi, M., Madanipour, S., and Taghilou, B. (2017). Structural control on overprinting high-sulfidation epithermal on porphyry mineralization in the Chodarchay deposit, northwestern Iran. *Ore Geol. Rev.* 86, 212–224. doi:10.1016/j.oregeorev.2017.01.028

Yu, D., Xu, D., Wang, Z., Xu, K., Huang, Q., Zou, S., et al. (2021). Trace element geochemistry and O-S-Pb-He-Ar isotopic systematics of the Lishan Pb-Zn-Cu hydrothermal deposit, NE Hunan, South China. *Ore Geol. Rev.* 133, 104091. doi:10.1016/j.oregeorev.2021.104091

Zamanian, H., Rahmani, S., and Zareisahameih, R. (2019). Fluid inclusion and stable isotope study of the Lubin-Zardeh epithermal Cu-Au deposit in Zanjan Province, NW Iran: Implications for ore Genesis. *Ore Geol. Rev.* 112, 103014. doi:10.1016/j.oregeorev.2019.103014

Zhai, D., Liu, J., Zhang, H., Tombros, S., and Zhang, A. (2018). A magmatic-hydrothermal origin for Ag-Pb-Zn vein formation at the Bianjiadayuan deposit, inner Mongolia, NE China: Evidences from fluid inclusion, stable (C-H-O) and noble gas isotope studies. *Ore Geol. Rev.* 101, 1–16. doi:10.1016/j.oregeorev.2018.07.005

Zhai, W., Sun, X., Sun, W., Su, L., He, X., and Wu, Y. (2009). Geology, geochemistry, and Genesis of Axi: A Paleozoic low-sulfidation type epithermal gold deposit in Xinjiang, China. *Ore Geol. Rev.* 36 (4), 265–281. doi:10.1016/j.oregeorev.2009.04.003

Zhao, D., Han, R. S., Wang, L., Ren, T., Wang, J. S., Zhang, X. P., et al. (2021). Genesis of the Lehong large zinc–lead deposit in northeastern Yunnan, China: Evidences from geological characteristics and C-H-O-S-Pb isotopic compositions. *Ore Geol. Rev.* 135, 104219. doi:10.1016/j.oregeorev.2021.104219

Zheng, Y. F. (1999). Oxygen isotope fractionation in carbonate and sulfate minerals. *Geochem. J.* 33, 109–126. doi:10.2343/geochemj.33.109

Zhong, J., Chen, Y. J., Chen, J., Qi, J. P., and Dai, M. C. (2018). Geology and fluid inclusion geochemistry of the Zijinshan high-sulfidation epithermal Cu-Au deposit, Fujian Province, SE China: Implication for deep exploration targeting. *J. Geochem. Explor.* 184, 49–65. doi:10.1016/j.gexplo.2017.10.004